University of Kentucky

UKnowledge

2024

MEASUREMENT AND SIMULATION OF AEROACOUSTIC SOURCES GENERATED BY ELEMENTARY MUFFLER COMPONENTS

Seth Donkin
University of Kentucky, sdonkin93@gmail.com
Digital Object Identifier: https://doi.org/10.13023/etd.2024.336

Right click to open a feedback form in a new tab to let us know how this document benefits you.

Recommended Citation

MEASUREMENT AND SIMULATION OF AEROACOUSTIC SOURCES
GENERATED BY ELEMENTARY MUFFLER COMPONENTS

_____

THESIS

_____

A thesis submitted in partial fulfillment of the
requirements for the degree of Master of Science in
Mechanical Engineering in the College of Engineering
at the University of Kentucky

By

Seth Donkin

Lexington, Kentucky

Director: Dr. David W. Herrin, Professor of Mechanical Engineering

Lexington, Kentucky

2024

ABSTRACT OF THESIS

MEASUREMENT AND SIMULATION OF AEROACOUSTIC SOURCES GENERATED BY ELEMENTARY MUFFLER COMPONENTS

Mufflers and silencers are commonly used to control noise from sources such as internal combustion engines and heating, ventilating, and air conditioning (HVAC) systems. In these applications, flow interacts with muffler components generating aeroacoustic noise sources. In order to measure these sources in a lab setting, specialized flow rigs are designed to isolate aeroacoustic noise sources. Flow sometimes compromises muffler performance. However, muffler performance is sometimes improved because flow can increase the attenuation of some muffler elements such as perforates. To better understand the complicated impact of flow, the University of Kentucky developed a muffler test rig to measure insertion loss and noise reduction with flow included. Additionally, the rig can be used to isolate and quantify the aeroacoustic sources inside of a muffler or at the termination. In this research, the test rig is first validated by measuring the aeroacoustic sources for a subsonic jet at the outlet of a straight pipe. Data is compared with theory to verify that the measured aeroacoustic sources match what is anticipated from well understood acoustic source power laws. The test rig is then used to measure the whistle tones generated by a perforated concentric tube resonator. The effect of hole diameter and porosity is evaluated. Finally, a subsonic jet is simulated using computational fluid dynamics and acoustic finite element analysis. The measured sound power is compared with the aeroacoustic simulation and correlation is excellent.

KEYWORDS: Flow-Induced Noise, Computational aeroacosustics (CAA), Silencers, Concentric Tube Resonator (CTR), Subsonic

Seth Donkin
Student's Signature

04/21/2024
Date

MEASUREMENT AND SIMULATION OF AEROACOUSTIC SOURCES
GENERATED BY ELEMENTARY MUFFLER COMPONENTS

By

Seth Donkin

Dr. David Herrin
Director of Thesis

Jonathan Wenk, Ph. D
Director of Graduate Studies

07/30/2024
Date

TABLE OF CONTENTS

LIST OF TABLES

LIST OF FIGURES

CHAPTER 1. INTRODUCTION

1.1   Background

Noise pollution is a pervasive issue that affects various aspects of life. In some cases, it can detrimentally impact one's health. Thus, commercial pressure and regulatory action has forced industry to develop equipment and machinery having lower noise emissions. This is especially the case in the automotive, aerospace, and power industries where the primary noise generating components are rotating machinery such as internal combustion engines (ICE), turbines, compressors, and fans. These components produce noise in two ways. The combustion or pumping process is the primary source of noise that must be dealt with using a muffler. Secondly, the equipment generates high flow, which inevitability produces noise as it interacts with the structures of the muffler and the surroundings.

Flow affects a muffler's performance in two ways. First, the flow will modify the acoustic performance of muffler elements. This can sometimes positively impact the muffler's performance. For example, the acoustic resistance of a perforated plate or tube increases with flow. Secondly, the flow through the muffler and piping can produce aeroacoustic noise sources in addition to the primary source. Depending on the underlying mechanism generating the aeroacoustic noise, the resulting sound can be broadband, such as air rushing out of a vent, or narrowband, such as the noise generated by a whistle. Broadband noise will be the major concern when trying to meet regulatory requirements, while narrowband noise contributes significantly to customer satisfaction due to the increased annoyance factor. The impact of aeroacoustic noise sometimes

necessitates thorough investigation and mitigation strategies by noise control engineers. In this context, accurate measurement and simulation techniques are essential for understanding the underlying physical phenomena, predicting noise levels, and designing efficient noise reduction strategies.

Muffler performance is typically measured using a transmission or insertion loss test rig or by measuring insertion loss on the actual product. Measurements are normally made without flow. Hence, it is assumed that flow will not affect the performance. However, this assumption is not appropriate in many applications.

The simplest and most used form of these rigs is a modified impedance tube with two microphones on each side of the muffler element under test. These simple rigs are aimed at determining the transmission loss without flow by measuring the incident and transmitted sound power of the measured system. If flow is included, far more sophisticated systems are required. One of the earliest flow rigs was developed by Sullivan [1] who measured transmission loss with flow by attaching a crude anechoic termination downstream of the muffler. Researchers at KTH, developed a more sophisticated muffler transmission loss flow rig that Elnady [2] further developed and commercialized. The KTH and Elnady rig uses the two-source method for determining transmission loss. Loudspeakers are attached to the sides of the tubes on both the inlet and outlet sides of the muffler system. The flow source is either a wind tunnel or blower, and flow noise from the flow source is attenuated using a large silencer. This silencing of the aeroacoustic noise from the flow source permits researchers to isolate the aeroacoustic noise generated from the muffler system. Researchers at Ohio State

University [3] developed a similar rig using the alternative two-load approach in which the acoustic load (i.e., the termination) is modified.

All these rigs are designed to measure transmission loss with flow. In academia, transmission loss is normally of greater interest because the muffler is characterized independent of the system it is installed in, and transmission loss is convenient for direct comparison with an acoustic simulation. However, an insertion loss rig is of greater interest in industry because that is the metric commonly measured in the field. Measuring insertion loss significantly simplifies the measurement, as measurements do not have to be taken inside the duct where flow can corrupt the measurements or damage microphones. Due to the interest in insertion loss and flow generated noise, the University of Kentucky has been engaged in a multi-year project to develop an insertion loss test rig. This test rig is based on a rig first developed by Sullivan [1] and adapted by Howell [4]. Chen [5] designed and qualified the test rig at the University of Kentucky to measure insertion loss with and without flow, transmission loss without flow, and noise reduction without flow.

One major advantage of the University of Kentucky's (UKy) muffler flow rig is the large silencer downstream of the blower. The silencer is effective at attenuating noise above 250 Hz and so the source noise from the blower is largely eliminated. Additionally, the flow source and silencer combination is absorbing so that sound waves reflected back upstream from the muffler system are absorbed. Thus, the flow noise source from the blower (e.g., the blade pass frequency) and the pipe resonances are largely eliminated at high frequencies. With these sources of contamination reduced, the test rig is an ideal candidate for measuring aeroacoustic noise phenomenon produced by flow in muffler

systems. Thus, this research will initially focus on the qualification of the test rig to measure aeroacoustic phenomena caused by the internal geometry of the intake or exhaust muffler system. Two types of aeroacoustic sources will be examined. First, the aeroacoustic sources generated at the end of an exhaust outlet will be measured. Secondly, the sources which arise due to a concentric perforated tube resonator will be characterized.

The UKy muffler test rig should provide valuable insight into aeroacoustic noise sources. Since few similar rigs are available, measurements using the UKy muffler test rig will be correlated with aeroacoustic simulation which is more widely used in industry. This will provide valuable benchmark results that other users can use to validate their simulations. Numerical simulation techniques, such as computational fluid dynamics (CFD) and computational aeroacoustics (CAA), have become significantly more accessible with increasing computational power. With the currently commercially available software packages, a standard workstation can be used to investigate complex flow-field and noise generation mechanisms. Thus, the final section of this work focuses on demonstrating the construction and validating the results of a CAA simulation using commercially available software.

1.2   Objectives

The objectives of this research are to:

1. Develop the procedures to measure flow generated noise using the UKy flow rig.

2. Validate the UKy rig by using it to measure noise generated by a subsonic jet. Measured results are correlated with published theory.

4

3. Measure and experimentally investigate the whistle due to flow passing through perforated pipes of concentric tube resonators at Mach numbers ranging from 0.05 to 0.25.

4. Use the results from Objective 3 to characterize the effect of porosity, hole diameter and flow velocity on the generated whistle noise from a perforated concentric tube resonator.

5. Validate a combined CFD and aeroacoustic FEM model of a subsonic jet using the data collected from the UKy muffler test rig.

1.3   Organization

Chapter 1 presents the objectives, and motivation for this research.

Chapter 2 details the background and theory used in validating the measurements and the construction of an aeroacoustic finite element model.

Chapter 3 details the research completed to validate the University of Kentucky's muffler test rig functionality in measuring flow noise phenomena.

Chapter 4 documents and summarizes the measurements of aeroacoustic noise generated by flow through a concentric tube resonator.

Chapter 5 details the construction and validation of an aeroacoustic finite element model of a subsonic jet.

Chapter 6 summarizes the findings of the research and offers recommendations for future work in improving the test rig and modeling techniques.

CHAPTER 2. BACKGROUND

2.1 Acoustic Sources

Lighthill identified three elementary acoustic sources: monopoles, dipoles, and quadrupoles. Monopole sources result from fluctuating volumes or mass flow. Dipole sources correspond to fluctuating forces and quadrupoles form because of fluctuating stress fields. As the order of the source increases, its efficiency as an acoustic source decreases. Thus, in cases with more than one form of elementary source present, the lowest order source will typically be dominant. Due to their minimal radiated acoustic power, higher order sources are typically not considered. In the work here, the highest order source considered will be the quadrupole.

2.1.1 Monopole

Monopole sources are the simplest acoustic source and radiate sound equally in all directions. Monopoles are typically formed due to pulsating flow such as the inlet and outlet flow of a reciprocating pump or the exhaust of a reciprocating engine. Other examples of monopole sources include tire noise, compressor noise, and loudspeakers at low frequencies. In practice, any source whose dimensions are significantly smaller than the wavelength of the emitted sound typically act as a monopole. The simplest form of a monopole is thus a small pulsating sphere with a diameter very much less than any generated wavelength. In the far-field at a distance of r such that $kr \gg 1$ the radiated pressure is expressed as

$$p(r, \theta, t) = j\rho_0 c_0 \frac{Qk}{4\pi} e^{j(\omega t - kr)} \qquad \text{2.1.1}$$

where ρ_0 is the fluid density of the acoustic medium, k is the wave number, c is the speed of sound in the acoustic medium, and ω is the angular frequency. Q is the root mean square (RMS) volume flux of the fluid produced at the source. In the case of a small pulsating sphere the RMS volume flux is given by

$$Q = 4\pi a^2 U_0 \qquad \text{2.1.2}$$

where a is the spheres radius and U_0 is the surface velocity of the sphere. In general, the volume flux of a monopole source is

$$Q = \iint \vec{u} \cdot \hat{n} dS \qquad \text{2.1.3}$$

where $\vec{u}$ is the velocity at a point on the sources surface.

The radiated sound power of a monopole source is given by

$$W_M = \rho_0 c_0 \frac{Q^2 k^2}{4\pi(1 + k^2 a^2)}. \qquad \text{2.1.4}$$

In the case of a pulsating flow such as that found at the tailpipe of a reciprocating engine or compressor inlet it can be assumed that

$$Q \propto SU \qquad \text{2.1.5}$$

where S is the cross-sectional area of the inlet or outlet, and U is the local mean flow velocity. The wave number, which is equivalent to ω/c_0 must likewise be proportional to

the U divided by the characteristic length of the source. The characteristic length squared is proportional to S

$$k^2 \propto \frac{U^2}{S c_0^2} \qquad\qquad 2.1.6$$

Using the relations given in Equations 2.1.5, 2.1.6 and the radiated sound power of a monopole source as given in Equation 2.1.4 the following is derived:

$$W_M \propto \frac{S \rho_0 U^4}{c_0} \propto S \rho_0 U^3 M \qquad\qquad 2.1.7$$

Equation 2.1.7 shows that the sound power of an aeroacoustic monopole source is expected to increase with the fourth power of the flow velocity. For subsonic ($M < 1$) flows, $S \rho_0 U^4$, a measure of the flows converted kinetic energy, can be interpreted as a measure of the source efficiency.

2.1.2   Dipole

Dipoles are constructed of two opposite phase monopoles placed close together at a small distance, $2h$. In aeroacoustics, dipole sources are typically generated due to flow over small obstructions in a stream and the resulting vortex shedding. Examples include flow over a rod and propellers. The pressure radiated by a dipole source according to Bies [6] is expressed as

$$p(\boldsymbol{r}, \theta, t) = -j \rho_0 c_0 \frac{Q k^2 l}{4 \pi r} \cos \theta \, e^{j(\omega t - kr)} \qquad\qquad 2.1.8$$

where r and θ define the position of the receiver as given in Figure 2-1.
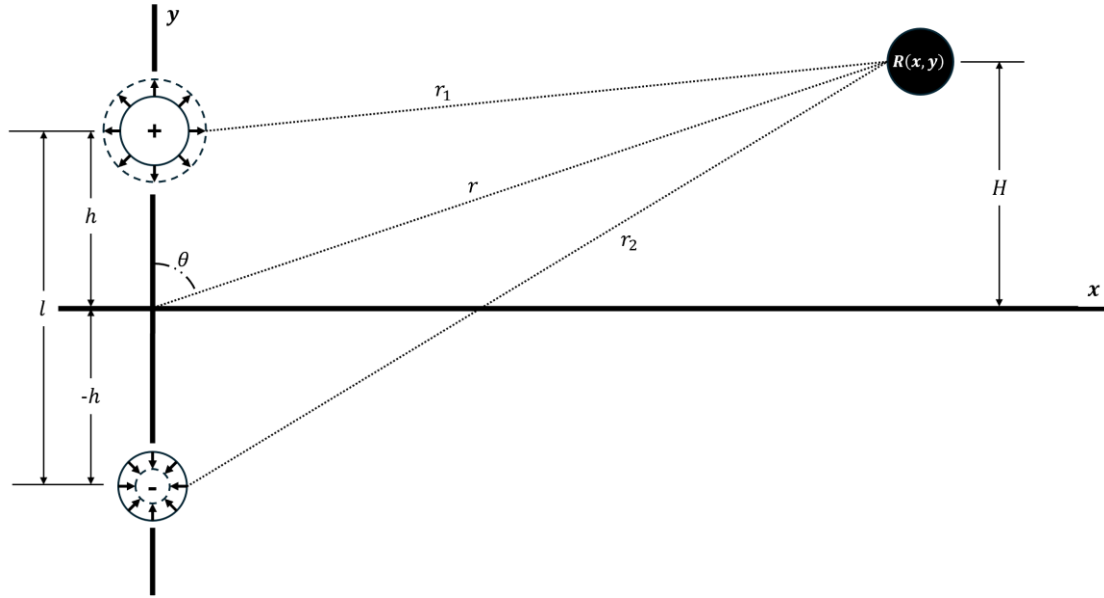
Figure 2-1 Illustration of a dipole source, and the position of the reciever, R, relative to the source in cartiesian coordinates. The sound pressure from the dipole source at R is defined by Equation 2.1.8.

The radiated sound power of a sphere of radius a encompassing a dipole source is given by

$$W_D = \rho_0 c_0 \frac{k^4 l^2 Q^2}{12\pi(1 + k^2 a^2)} \qquad 2.1.9$$

As with the monopole source, Equations 2.1.5 and 2.1.6 apply for an aeroacoustic dipole source such as a small obstruction in a fluid stream. Substitution of these relations into Equation 2.1.9 gives

$$W_D \propto S\rho_0 U^6 c_0^3 \propto S\rho_0 U^3 M^3 \qquad 2.1.10$$

Hence, the sound power of an aeroacoustic dipole source is proportional to the flow velocity to the sixth power of the flow velocity. A dipole's efficiency in the case of a subsonic flow is proportional to $S\rho_0 U^6$. This interpretation shows that a dipole source is

9

significantly less effective than a monopole source at converting flow stream kinetic energy to sound. However, the dipole source's efficiency increases more rapidly with the flow velocity than the monopole source.

2.1.3 Quadrupoles

Quadrupole sources consist of two dipoles of the same strength with opposite phase separated by a distance D. Quadrupoles arise from turbulence and generate sound waves through a fluctuating stress field acting on an acoustic medium. The turbulence in a jet is the textbook example of a quadrupole source. Depending on the configuration of the two dipoles, quadrupoles can be further classified as either longitudinal or lateral. Longitudinal quadrupole sources correspond to tensional or compressive stress and the dipole axes lie along the same line, as shown in Figure 2-2a. A lateral quadrupole source is caused by shear stresses, and the dipole axes are parallel to one another, as shown in Figure 2-2b. In spherical coordinates the far field sound pressure for both a longitudinal and lateral quadrupole are expressed as

$$p_{longitudinal} = -\rho_0 c_0 \frac{k^2 Q \omega 2hD}{4\pi r} \cos^2 \theta \qquad 2.1.11$$

$$p_{lateral} = -\rho_0 c_0 \frac{k^2 Q \omega 2hD}{4\pi r} \cos \theta \sin \theta \cos \phi \qquad 2.1.12$$

where, θ, r, and φ define the receiver position, R, respective of the source as shown in Figure 2-3.

The radiated sound power of sphere of radius a enclosing a longitudinal or a lateral quadrupole are expressed by Equations 2.1.13 and 2.1.14, respectively.

$$W_{longitudinal} = \rho_0 c_0 \frac{4k^6 h^2 D^2 Q^2}{5\pi(1 + k^2 a^2)})$$ 2.1.13

$$W_{lateral} = \rho_0 c_0 \frac{4k^6 h^2 D^2 Q^2}{15\pi(1 + k^2 a^2)})$$ 2.1.14
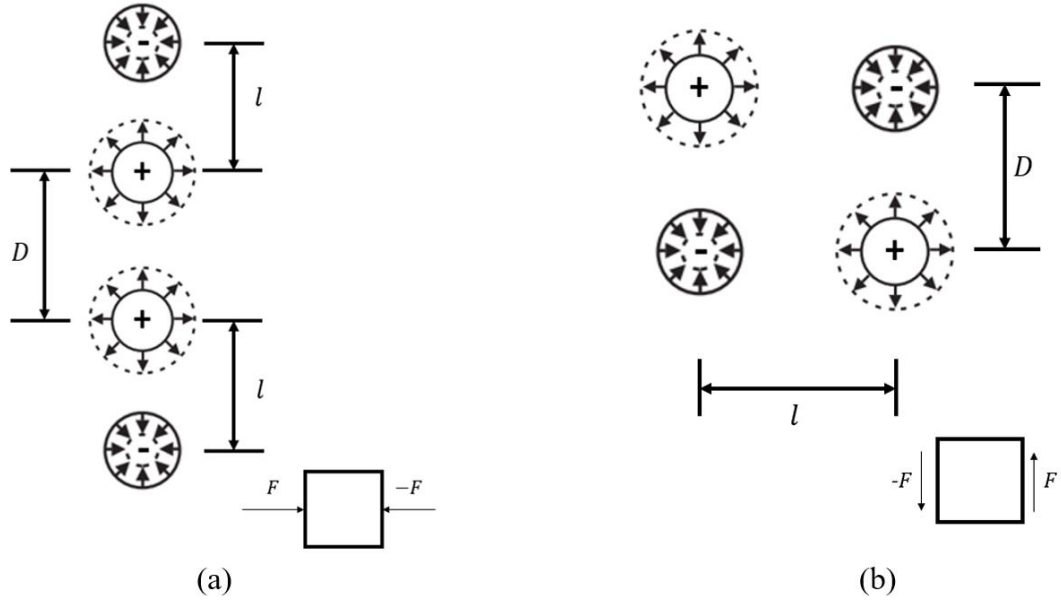
Figure 2-2 Illustration of a (a) longitudinal and (b) lateral quadrupole sources with their respective equivalent stress models.

By applying the relationships given in Equations 2.1.5 and 2.1.6 to either

Equation 2.1.13 or 2.1.14, the proportionality relationship for quadrupole sound power

can be expressed as

$$W \propto S\rho_0 U^8 c^5 \propto S\rho_0 U^3 M^5$$ 2.1.15

Thus, the sound power of a quadrupole source is proportional to flow velocity to the

eighth power for subsonic flow. The radiated power from a quadrupole source due to a

subsonic flow is then proportional to the $S\rho_0 U^8$. A quadrupole source is a less effective

radiator than either a dipole or monopole, but its efficiency increases more rapidly with

11

the flow velocity than either a dipole or monopole source. Consequently, a quadrupole

source is commonly masked by either a monopole or dipole source.
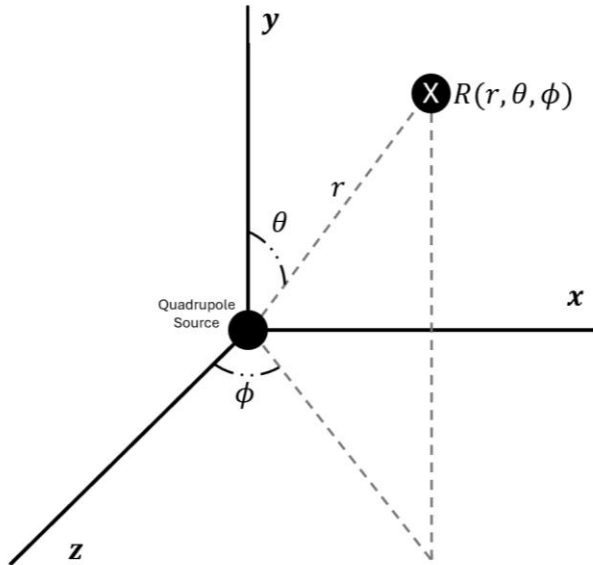
Figure 2-3 Diagram of a receivers position, R, respective to a quadrupole source in polar coordinates. The sound pressure at R from the quadrupole source at $(0,0,0)$ is defined by Equation 2.1.11 or 2.1.12.

2.2 Lighthills Analogy

Dr. Michael James Lighthill is commonly referred to as the father of aeroacoustics. His founding paper *On sound generated aerodynamically, I. General Theory* [7] was published in 1952. Since Lighthill's initial publication, aeroacoustics has become a branch of acoustics studying sound induced by aerodynamic phenomena and fluid flow. In the 70 years since, Lighthill's initial theories have been substantially developed and widely applied in modern engineering.

Lighthill's famous work is focused on the sound generated aerodynamically, a byproduct of turbulent flow and distinct from sound generated by the vibration of a solid

medium. Lighthill estimated the radiated sound from a given fluctuating fluid flow also commonly referred to as a turbulent flow. To deal with the problem, Lighthill divided the fluid into a source and acoustic domain and applied assumptions to each domain. The source domain contains the real fluid flow which is a nonuniform medium not at rest. The acoustic domain is a uniform medium at rest further simplified under the assumption that it is a free field. The second assumption Lighthill makes is to neglect acoustic propagation in the source domain. His third and final assumption is that the acoustic domain has no back-reaction on the source domain. Lighthill's three assumptions are applicable to most engineering problems. The major exceptions are in the cases of resonators or cavities close to the fluid flow, or when the flow velocity exceeds Mach 0.3[8][9].

Under his three assumptions, Lighthill begins by comparing the equations governing the fluctuations in density of the two domains. Inside the source domain, the density fluctuations of the real fluid are defined as a combination of the momentum flux tensor, the hydrostatic pressure and the viscous stresses at the boundary of the domain. The acoustic domain experiences density fluctuations as a simple hydrostatic pressure field. The difference between the density fluctuations of the source and acoustic domains is then used to define a force field on the boundary of the source domain acting on the acoustic domain. Acoustic metrics can then be predicted inside the acoustic domain by solving the Helmholtz equation. As a result of assuming the acoustic domain is a free field, the Helmholtz equation can be easily solved using numerical simulation.

2.2.1   Development of Lighthills Analogy

For a fluid the continuity and momentum equations are expressed as:

$$\frac{\delta \rho_0}{\delta t} + \frac{\delta}{\delta x_i}(\rho_0 v_i) = 0 \qquad\qquad 2.2.1$$

$$\frac{\delta}{\delta t}(\rho_0 v_i) + \frac{\delta}{\delta x_j}(\rho_0 v_i v_j + p_{ij}) = 0 \qquad\qquad 2.2.2$$

Here, v_i and v_j is the velocities in the two perpendicular directions x_i and x_j. p_{ij} is a compressive stress tensor describing the hydrostatic and viscous stresses at the boundary.

It is straightforward to eliminate the momentum density ρv_i and obtain,

$$\frac{\delta^2 \rho_0}{\delta t^2} = \frac{\delta^2}{\delta x_i x_j}(\rho_0 v_i v_j + p_{ij}) \qquad\qquad 2.2.3$$

where the right-hand side term $\rho v_i v_j + p_{ij}$ fully describes density fluctuations in the fluid domain, $p v_i v_j$ describe the momentum flux inside of the fluid domain and are commonly referred to as the Reynolds stresses. The density of the acoustic domain is then accounted for by subtracting $c_0^2 \frac{\delta^2}{\delta x_i^2}$ from both sides resulting in,

$$\frac{\delta^2 \rho_0}{\delta t^2} - c_0^2 \frac{\delta^2 \rho_0}{\delta x_i^2} = \frac{\delta^2}{\delta x_i x_j}(\rho_0 v_i v_j + p_{ij} - c_0^2 \rho_0 \delta_{ij}) \qquad\qquad 2.2.4$$

where δ_{ij} is the Kronecker delta and $c_0^2 \rho \delta_{ij}$ describes the fluctuations in the density of the acoustic domain as a simple hydrostatic pressure field.

Equation 2.2.4 is equivalent to the wave equation with a source term on the right-hand side and is referred to as Lighthill's Equation. The source term is the difference between the density fluctuations in the fluid and acoustic domain and is expressed as

$$T_{ij} = \rho_0 v_i v_j + p_{ij} - c_0^2 \rho_0 \delta_{ij} \qquad\qquad 2.2.5$$

14

which is referred to as the Lighthill stress tensor. This tensor describes the strength per unit volume of a distribution of sound sources inside of the fluid domain.

The problem can be simplified by approximating the Lighthill stress tensor as

$$T_{ij} \approx \rho_0 v_i v_j \qquad \text{2.2.6}$$

This approximation is applicable to cases in which the following conditions apply:

- Low Mach Number – velocity fluctuations are of the order $\rho_0 M c_0^2$,

- High Reynolds Number – viscous effects are significantly smaller than the inertial effects, and the Reynolds stresses are much higher than the viscous stresses,

- Isentropic flow,

- Viscous stress terms, $-\sigma_{ij} = \mu \frac{\delta v_i}{\delta x_j}$, in T_{ij} can be neglected as they correspond to the very ineffective octupole sound source expressed as

  $\frac{\delta^2 T_{ij}}{\delta x_i x_j} = \frac{\delta^3 v_i}{\delta x_i \delta x_j \delta x_k}$.

Finally, Lighthill's equation is converted to the frequency domain and written as,

$$-\omega^2 \rho_0 - c_0^2 \frac{\delta^2 \rho_0}{\delta x_i^2} = \frac{\delta^2 T_{ij}}{\delta x_i \delta x_j} \qquad \text{2.2.7}$$

2.2.2 Dimensional Analysis of Lighthill's Equation

Lighthill proceeded to formulate the total acoustic power output, and through dimensional analysis he formulates that the acoustic power of a quadrupole source is equivalent to turbulence in a free space as defined by

$$W \propto \rho_0 U^8 c_0^{-5} L^2 \qquad\qquad 2.2.8$$

where U is the flow velocity and L is the characteristic length of the flow. As noted in the

prior section, acoustic power of quadrupole sources is proportional to flow velocity to the

eighth power. This relationship between the flow velocity and the quadrupoles

equivalency to free space turbulence is commonly referred to as the 8th power rule [9].

2.2.3   Application to Aerodynamic Sources Inside of Pipes and Ducts

Though applicable in many cases, Lighthill's original formulation is limited to

aeroacoustic sources within a free field. To begin formulating the impact of solid

boundaries on aeroacoustic sources one must consider that their presence physically

impacts the acoustic sources in two ways:

i.   Reflection of the sound generated by the quadrupoles will be reflected and
       diffracted.

ii.   The distribution of the quadrupole sources is limited to the region external to
       the solid boundaries. At the fluid and solid interface, the forces on the fluid
       from the solid will likely equate to a distribution of dipoles since, as discussed
       in the previous section, dipole sources occur in cases of externally applied
       forces on a medium.

From these assumptions, Curle [10] was one of the first to modify Lighthill's

Analogy by adding the impact of solid boundaries on the sound field generated by a

limited region of turbulence. Curle's formulation assumes the solid boundaries are fixed

or only vibrate in their own plane. Thus, the sound generated in the surrounding at rest

fluid is equivalent to a distribution of dipole sources with equivalent strength to the force

16

per unit area exerted on the fluid by the solid boundary in the normal direction. The sound field generated by a limited region of turbulence impeded by a solid boundary is the sum of a volume distribution of quadrupole sources and a surface of dipole sources. Through dimensional analysis, Curle then formulates that the total acoustic power output of a finite region of turbulence impeded on by a finite solid body is defined by the proportionality,

$$W \propto \rho_0 U^6 c_0^{-3} L^2 \qquad\qquad 2.2.9$$

where L is the characteristic dimension of the solid boundary and U is velocity of the fluid.

Davis and Ffowcs William [11] further adapted the work of Curle to the case of turbulence contained within a hard walled pipe. Inside of the pipe, the generated sound field is equivalent to a line of dipole sources. The rigid walls of the pipe were found to have a substantial effect on the radiation efficiency of these sources. The sound generated by the large-scale turbulence, when motion is completely correlated across the pipe, is in the form of a plane wave and increases with the sixth power of the flow velocity. Thus, the energy radiated by the large-scale turbulence exceeds the same turbulence in a free space by a factor of $1/M^2$. This holds for small-scale turbulence of low frequency when only the plane wave propagates and other modes inside the pipe decay exponentially with distance. In both the cases of large-scale turbulence and low frequency small-scale turbulence, convection effects result in a large increase in the acoustic power of the turbulent sources. In the case of high frequency small-scale turbulence, all acoustic modes are excited, and the turbulence radiates in the same way as if it was in free space. Finally, Davis and Ffowcs Williams assumed that the turbulence inside the pipe is

approximately $1/10th$ of the pipes width. Thus they formulated that for flow velocities

less than Mach 0.2, the sound power of the turbulence is proportional to U^6 which

corresponds to a dipole source. Above Mach 0.2 the turbulence acts as if in a free space

and is proportional to U^8 which corresponds to quadrupole sources.

2.3   Computational Fluid Dynamic (CFD) Turbulence Models

If a faucet is slightly turned on, the water runs gradually and smoothly into the

drain. As the faucet is opened further, the flows velocity increases and the flow pattern

becomes more complicated. This complex flow pattern is called turbulent flow and the

former is laminar flow. In the case of turbulent flows, circular motions that move counter

to the main current develop and the rate of heat transfer increases. These circular motions

are called turbulent eddies and they promote mixing within the fluid.

The distinction between laminar and turbulent flow was introduced by the 1883

experiments of British scientist Osboren Reynolds [12]. By observing injected ink into

water flowing through a pipe, Reynolds observed two different flow states; laminar flow

in which the ink flowed in a straight line, and turbulent in which the ink mixed within the

pipe. To predict the transition of flow between these two states, Reynolds used the ratio

of the fluid's viscosity, μ, and the velocity, u. This new dimensionless parameter was

deemed the Reynolds Number and is define as

$$Re = \frac{\rho_0 uL}{\mu}$$
<div align="right">2.3.1</div>

where L is the characteristic length of the flow. The Reynolds number is the ratio of the

viscous forces to the inertial forces. Flow will be laminar in pipes if the Reynolds number

is below 2000, and it will be fully turbulent if the Reynolds number exceeds 4000. In general, most flow is turbulent with some exception of very low velocity flows like natural convection inside of electronics.

The eddies in turbulent flow occur in many sizes, stimulate the momentum exchange, and affect the velocity distribution of the flow. To numerically analyze the flow accurately, the capturing of the eddies and/or their effect is necessary. Simulation of one eddy requires at least nine elements for a two-dimensional representation, as shown in Figure 2-4, and at least twenty-seven for a three-dimensional representation. The task of capturing the eddies is further complicated because eddies break down into smaller eddies with several scale levels until finally dissipating into heat energy. This process of decomposition is diagrammed in Figure 2-5.
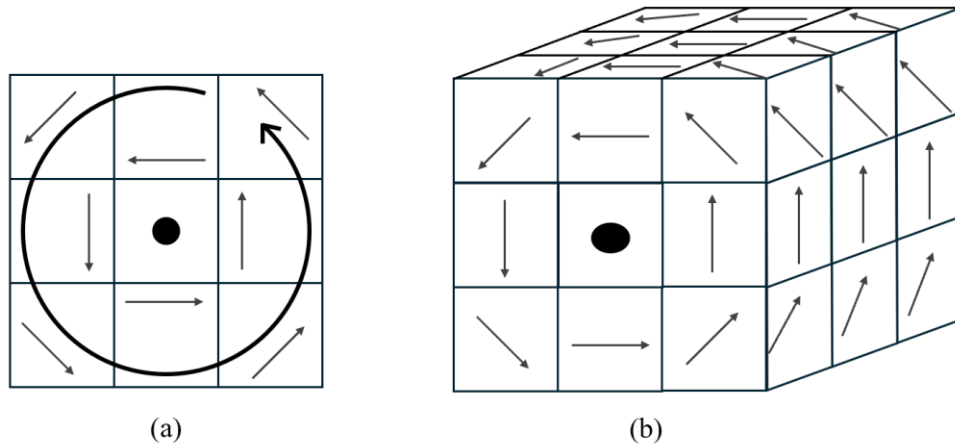
Figure 2-4 Illustration of the number elements required to capture a single eddy in (a) 2D and (b) 3D. In 2D nine elements are required to capture an eddy. To capture an eddy in 3D the 27 elements are required.
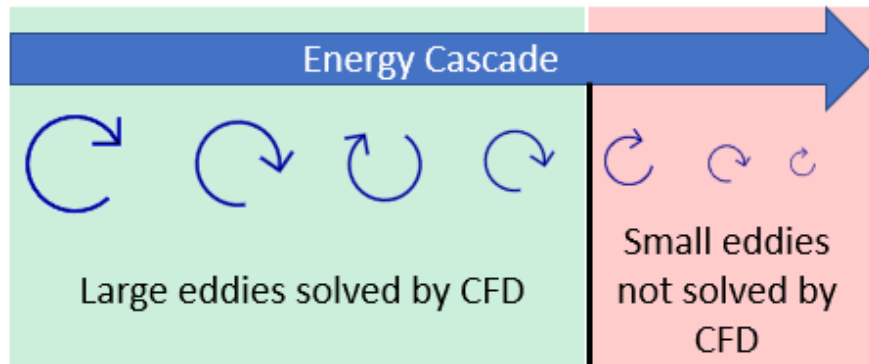
Figure 2-5 Illustration of eddy size and energy cascade as eddy dissipates.

2.3.1 Reynolds Averaged Navier-Stokes (RANS) Models

Since turbulent flow is made up of large numbers of eddies and vortices, it is

nearly impossible and impractical to directly simulate using current computational

resources. For most engineering applications, the microscopic structures of the eddies do

not need to be modeled. However, their effect on mean velocity distribution and heat

transfer must be considered. Under these assumptions, the Reynolds Averaged Navier-Stokes (RANS) CFD methodology averages the turbulent flow over a duration of time to obtain a time-averaged steady-state solution. The effect of the turbulence is accounted for using a turbulence model. Turbulence models can capture the effects of small eddies without directly modeling the motion which significantly reduces the number of required mesh elements. RANS models thus have remarkably reduced computational cost compared to other methods.

Turbulence models address the Reynolds stress, the turbulent thermal conductivity, κ_t, and the turbulent diffusion coefficient, D_{mt}. The Reynolds stress can be assumed to be proportional to the spatial gradient of the mean velocity with a proportionality constant specified as the eddy viscosity, μ_t. From the eddy viscosity the turbulent thermal conductivity and diffusion coefficient can be found using

$$\kappa_t = \frac{\mu_t C_p}{P_{rt}}$$

2.3.2

$$D_{mt} = \frac{\mu_t}{\rho_0 S_{ct}}$$

2.3.3

where C_p is the specific heat of the fluid under constant pressure, P_{rt} is the turbulent Prandtl number and S_{ct} is the Schmidt number typically equal to 0.9. Thus, turbulent models use fundamental qualities of turbulence to determine the eddy viscosity, which in turn allows for the effects of the turbulence to be formulated.

2.3.1.1   k-epsilon (k $-$ ε) Turbulence Model

There is no single turbulence model which is valid for all turbulent phenomena. The $k - \varepsilon$ model is the most used turbulence model in industry because of its stability and convergence. W.P. Jones and Launder [14] first proposed the standard $k - \varepsilon$ model with the objective of improving the mixing-length hypotheses and avoid prescribing the turbulence length scale algebraically.

This semi-empirical model uses two fundamental qualities of turbulence to determine the eddy viscosity by solving their equations for advection, diffusion, formation, and consumption. The first fundamental quality is the turbulence energy defined as

$$k = \frac{1}{2} u_i' u_i' \qquad\qquad 2.3.4$$

where u_i' is the time-average of the velocity fluctuations in the ith direction. The second fundamental quality is the turbulence dissipation rate defined as

$$\varepsilon = v \frac{\delta u_i'}{\delta x_j} \frac{\delta u_i'}{\delta x_j} \qquad\qquad 2.3.5$$

The equations for the advection, diffusion, formation, and consumption for these two fundamental quantities of turbulence define the turbulence model. For an incompressible fluid, they are expressed as

$$\frac{\delta \rho_0 k}{\delta t} + \frac{\delta u_i \rho_0 k}{\delta x_i} = \frac{\delta}{\delta x_i}\left(\frac{\mu_t}{\sigma_k}\frac{\delta k}{\delta x_i}\right) + G_S + G_T - \rho_0 \varepsilon \qquad\qquad 2.3.6$$

$$\frac{\delta \rho_0 \varepsilon}{\delta t} + \frac{\delta u_i \rho \varepsilon}{\delta x_i} = \frac{\delta}{\delta x_i}\left(\frac{\mu_t}{\sigma_k}\frac{\delta \varepsilon}{\delta x_i}\right) + C_1\frac{\varepsilon}{k}(G_S + G_T) - C_2\frac{\rho_0 \varepsilon^2}{k} \qquad\qquad 2.3.7$$

$$G_S = \mu_t \left(\frac{\delta u_i}{\delta x_j} + \frac{\delta u_j}{\delta x_i} \right) \frac{\delta u_i}{\delta x_j} \qquad \text{2.3.8}$$

$$G_T = g_i \eta \frac{u_t}{\sigma_t} \frac{\delta T}{\delta x_i} \qquad \text{2.3.9}$$

where g_i is the acceleration due to gravity, η is the thermal expansion coefficient of the fluid, and empirical constants $\sigma_k, \sigma_\varepsilon, C_1, C_2, \sigma_t$ are 1, 1.3, 1.44, 1.92, and 0.9 respectively. Using Equations 2.3.4, 2.3.5 and dimensional analysis, the eddy viscosity is then found to be

$$\mu_t = C_\mu \rho_0 \frac{k^2}{\varepsilon} \qquad \text{2.3.10}$$

where the empirical constant C_μ is 0.09.

Equations 2.3.6 and 2.3.7 are the standard $k - \varepsilon$ equations and the constants which appear in them were established by experiment. The $k - \varepsilon$ model is only suitable for high Reynolds number flows and is most suitable for fully developed flow which is sufficiently spaced from wall boundaries. The model's performance in near-wall fields can be improved through the application of damping function.

2.3.1.2   k-omega ($k - \omega$)Turbulence Model

Kolmogorov [15] first introduced the $k - \omega$ turbulence model. Since its initial formulation, the model has been improved upon by several researchers. The most widely used version today, and the version implemented in this work, is based upon Wilcox et al [16] [17] [18]. The standard $k - \omega$ model uses the dissipation rate per unit of turbulent energy, ω, to solve for the eddy viscosity. The eddy viscosity is expressed as

$$\mu_t|_{k-\omega} = \rho_0 \frac{k}{\omega} \qquad\qquad 2.3.11$$

and k and ω are solved for using

$$\frac{\delta \rho_0 k}{\delta t} + \frac{\delta u_i \rho_0 k}{\delta x_i} = \frac{\delta}{\delta x_i}\left[\left(\mu + \frac{\mu_t}{\sigma_k}\right)\frac{\delta k}{\delta x_i}\right] + G_S + G_T - \rho_0 C_\mu k\omega \qquad 2.3.12$$

$$\frac{\delta \rho_0 \omega}{\delta t} + \frac{\delta u_j \rho_0 \omega}{\delta x_j}$$

$$= \frac{\delta}{\delta x_j}\left[\left(\mu + \frac{\mu_t}{\sigma_k}\right)\frac{\delta \omega}{\delta x_j}\right] + \left(\frac{\beta}{C_\mu} - \frac{\kappa^2}{\sigma_\omega \sqrt{C_\mu}}\right)\frac{\rho_0}{\mu_t}G_S - \beta\rho_0\omega^2$$

$$2.3.13$$

where constants $\sigma_k, \sigma_\omega, \beta$ and κ are equal to 1.18, 2.0, 0.075 and 0.41 respectively.

The k $-$ ω turbulence model reproduces near-wall behavior more accurately than the k $-$ ε model. However, the major disadvantage of the k $-$ ω turbulence model is the sensitivity of ω in Equation 2.3.13 outside of the boundary layer which leads to making the model being unreliable in the free stream [19]. This flaw prevents the k $-$ ω turbulence model from completely replacing the k $-$ ε turbulence model and has led to the development of the shear stress transport (SST) k $-$ ω turbulence model.

First developed in 1993 by Menter [20] the SST k $-$ ω turbulence model solves the standard k $-$ ω equations given in Equations 2.3.12 and 2.3.13 near the wall and then adjusts them to be equivalent to the k $-$ ε model in the outer regions.

The shifting between the k $-$ ω and k $-$ ε models is smoothed by the introduction of a blending function, whose arguments are the wall distance and turbulence quantities, multiplied by,

$$CD_{k\omega} = 2\frac{\rho_0}{\sigma_\omega \omega}\frac{\delta k}{\delta x_j}\frac{\delta \omega}{\delta x_j}. \qquad\qquad 2.3.14$$

The model's constants are given near-wall and outer region values which are then

interpolated using the blending functions. Table 2-1 lists the constants values for the

near-wall and outer region. Finally, the eddy viscosity for the SST $k - \omega$ turbulence

model is given as

$$\mu_t|_{SST} = \rho_0 \frac{a_1 k}{\Omega} \qquad\qquad 2.3.15$$

where constant a_1 is equal to 0.31 and Ω is the magnitude of the mean vorticity. In

practice the SST $k - \omega$ turbulence models offers both a more accurate and robust

computation than either the $k - \varepsilon$ or $k - \omega$ models do on their own.

Table 2-1 The values for the SST $k - \omega$ turbulence model's constants for the near-wall region and the outer region.

Constant	Near-Wall	Outer
C_μ	0.09	0.09
σ_k	1.18	1.0
σ_ω	2.0	1.17
β	0.075	0.0828

2.3.2   Large-scale Eddy Simulation (LES)

Many flow phenomenon, such as flow generated noise, cannot be evaluated using

time averaged characteristics. The evaluation of flow noise requires a method different

from RANS because of the temporal unsteadiness of turbulence and its relation to the

eddy motions. Large eddy simulations (LES) are one strategy for predicting the flow

characteristics that result in flow noise.

In LES, larger three-dimensional unsteady turbulent motions are directly solved, whereas smaller scale motions are modelled. This is accomplished by separating the Navier-Stokes equations into two parts, a filtered part, and a residual part. The larger unsteady turbulent motions are resolved in the filtered part while the residual part models the effects of the small-scale motions. Well documented explanations of the filtered Navier-Stokes equations can be found in many turbulence textbooks [21] and in documentation for commercial CFD solvers [13].

Large-scale turbulent motions mostly depend on the geometry and boundary conditions. The rate of energy transported from the larger scale eddies along with the viscosity determines the small-scale motions. The small-scale motion is captured using a sub-grid scale (SGS) model. As with RANS modeling, there are various SGS models to handle the indirectly modeled turbulence. For the work completed here, the Wall-Adapting Local Eddy Viscosity (WALE) model was used because it accurately captures the impact of eddy viscosity on near-wall motion and has a reduced calculation cost compared to other SGS models. The version of WALE model used in scFlow, the CFD solver used in this work, is described in Temmerman et. al. [22].

CHAPTER 3. MEASUREMENT APPROACH AND VALIDATION

The main objective of the measurements completed for this research is to develop

methodologies for repeatable and accurate data collection of noise generated by

aeroacoustic phenomena. The goal of such data is that it can be used for finite element

model validation and diagnosis of flow noise problems caused by either external or

internal elements of a muffler. Measurement methodologies were thus developed and

tested for accuracy using a subsonic jet from a straight pipe. Noise generated by subsonic

jets has been heavily researched, and the accuracy of the measurements in this work is

determined by testing their conformity to known theories discussed in Chapter 2.

3.1   Insertion loss

Insertion loss is one of the most common metrics used in industry to define a

muffler's performance. It compares the sound power levels from a source with a muffler

versus a baseline case. Typically, the baseline case will be a straight open pipe, but

another muffler can be used for a direct comparison. Insertion loss of a muffler is

dependent on the muffler's design and the impedances of the source and termination.

Thus, insertion loss is dependent on the system the muffler is connected to and will

change if the system changes. Due to this dependency on the system, insertion loss is best

determined experimentally and used as the final evaluation of a muffler design. Insertion

loss is expressed as

$$IL = L_W^{basline} - L_W^{muffler}$$ 3.1.1

where $L_W^{baseline}$ is the sound power level in dB at the outlet of the baseline case and $L_W^{muffler}$ is the sound power level in dB at the outlet with the muffler installed.

The measurement of insertion loss requires calculating the difference between the sound power level at the outlet of the baseline and muffler case. There are several methods for measuring sound power including approximating the sound power from sound pressure levels of several points in the acoustic field as shown in Figure 3-1. This method is preferable if an anechoic chamber can be used. In other cases, the sound power at the termination can be directly evaluated using sound intensity scanning.

If the sound pressure is sampled at various locations, multiple microphones are typically distributed at an equal distance from the outlet as shown in Figure 3-1. From the measure sound pressure, the sound power is calculated using

$$L_W = 10 \log_{10} \left[\frac{1}{N} \sum_1^N \left(\frac{p_i}{p_{ref}} \right)^2 \right] + 20 \log_{10} R \qquad 3.1.2$$

where R is the distance from the exhaust opening, N is the number of microphones, p_i is the measured pressure at the microphone, and p_{ref} is the reference pressure which for this work is defined as $20 \ \mu Pa$.
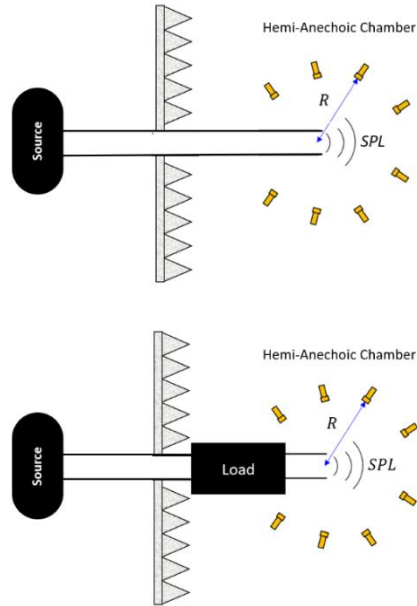
Figure 3-1 Diagram of the methodology used for measuring the insertion loss of by sampling at a collection of microphone measurement points in an anechoic chamber.

3.2 Measurement Setup

Measurements were performed using the muffler flow rig developed at the University of Kentucky shown in Figure 3-2. Flow is generated using a regenerative electric blower capable of withstanding back pressures up to 27.5 kPa (110 inH$_2$O). The velocity of the flow is determined using a pitot tube and a Dwyer Series 475 Mark III digital manometer. The flow is smoothed to increase the accuracy of the pitot tube by feeding it through a collection of soda straws. Chen [5] showed that this homemade flow conditioner allowed for the average flow rate to be estimated from the centerline velocity. Using the measured centerline velocity, the flow velocity at the inlet of the test muffler is estimated using Bernoulli's Equation.

To suppress the blower noise, a silencer with fiber lining the periphery is positioned after the flow conditioner. The fiber is held in place by a thin microperforated panel (MPP) tube which connects the inlet to the outlet pipe. This lining extends 122 cm. Figure 3-3 shows the silencer and its transmission loss with and without flow.
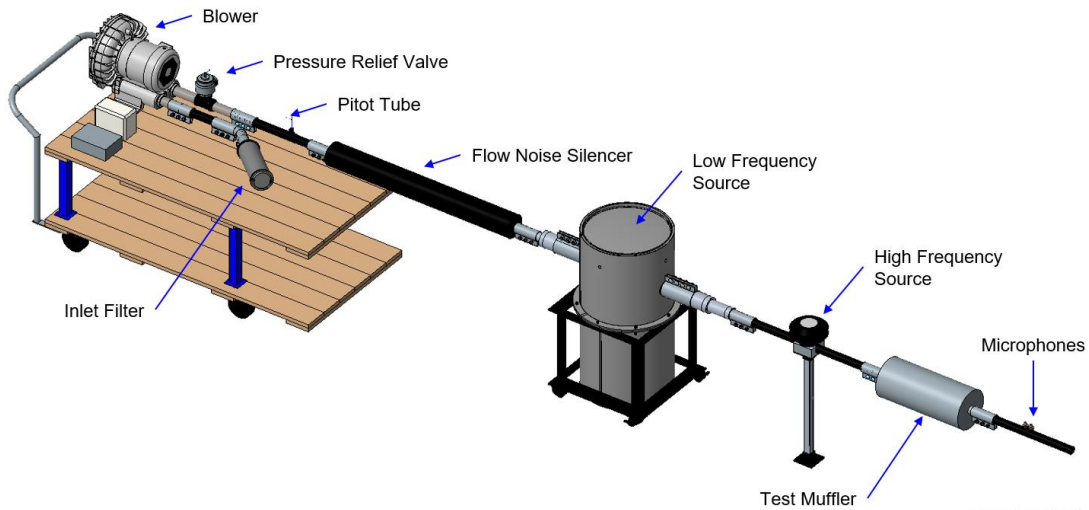
Figure 3-2 Schematic of the University of Kentucky's muffler flow rig.

(a)
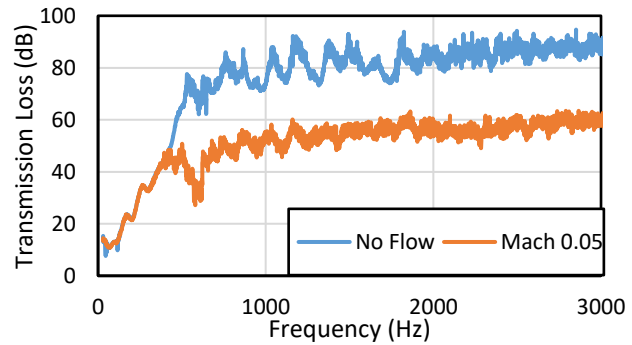
(b)

Figure 3-3 (a) An image of the silencer used to suppress noise from the blower. (b) The silencer's transmission loss sans flow and with a mean flow of Mach 0.05.

Further downstream, low and high-frequency sources are connected. The low-frequency source is a JBL 2226G subwoofer placed inside a large drum that generates

noise from 50 to 1200 Hz. An inverted horn is used to transition from the large diameter

subwoofer to the flow path. The high-frequency source is a JBL 2446H compression

driver flush mounted to the pipe. The test muffler is positioned downstream of the

sources. The end of the rig can then be modified to measure insertion loss, transmission

loss, and pressure drop.

Sound pressure is sampled on a hemisphere using eight ½-inch PCB free-field

microphones (Type 378A04). From the sound pressure measurements, the sound power is

calculated using Equation 3.1.2. An image of the 1.2 m microphone hemisphere is

shown in Figure3-4a. The blower and source are placed outside the hemi-anechoic

chamber, and the pipe feeds through a small opening in the chamber doors. As the pipe

prevents the anechoic chamber's bay doors from closing the aperture between the doors

is filled during measurements with sound absorption as shown in Figure 3-4b.

(a)   (b)

Figure 3-4 (a) The 1.2 m microphone hemisphere inside of the hemi-anechoic
chamber. (b) The sound absorption used to cover the small opening in the doors of the
hemi-anechoic chamber.

3.3   Validation of Measurement Quality – Straight Pipe Jet Case Study

To validate the rigs' ability to measure flow noise with minimal contamination from other sources, the sound produced by a subsonic jet at the outlet of pipes ranging in diameters between 0.875 to 2 inches was measured. To connect the test pipes with diameters less than 2 inches, a 12-inch-long 3D printed conical pipe adaptor is used. All test pipes are 4 ft (1.2 m) long to allow for turbulent flow to reform inside the pipe after the diameter reduction. The selected pipes have a wall thickness of 0.06 inches and have a smooth bore. Table 3-1 lists the tested flow velocities and dimensions of the four pipes. The flow velocities tested for each pipe were limited by the amount of back pressure the blower is rated for and the sensitivity of the manometer used for measuring the flow velocity.

Table 3-1 The dimensions and tested flow velocities of the four 4ft long sample pipes.

Pipe	Outer Diameter	Inner Diameter	Tested Flow Mach Numbers
A	2.22 cm (0.875 in)	1.89 cm (0.754 in)	0.45 0.4 0.35 0.3
B	2.86 cm (1.125 in)	2.53 cm (0.995 in)	0.35 0.3 0.25 0.2
C	4.13 cm (1.625 in)	3.80 cm (1.50 in)	0.25 0.2 0.15 0.1
D	5.08 cm (2 in)	4.75 cm (1.87 in)	0.15 0.1

By comparing the measured sound power of the subsonic jet to theory the accuracy of the flow noise measurement was determined. The existing theory for comparison includes that of Davies and Ffowcs Williams [11] and Curle [10] concerning

noise due to turbulence inside of an enclosed volume and Lighthill's formulation [7][8]

of the sound power of turbulence in a free space. Additionally, results are compared to a

predictive model provided in the German standard VDI3733[23] which provides acoustic

guidance on installation of circular cross-section pipes in industrial plants. A positive

correlation between the completed measurements indicates that the dominant source

measured is that caused by the turbulent flow.

3.3.1   Methodology for Comparing Measurement Data to Theory

From the theory discussed in sections 2.2.2 and 2.2.3, it is known that the acoustic

power from sources due to turbulence is directly proportional to the flow's velocity.

Thus, as flow velocity increases, the sound power of a particular source should increase

in a predictable manner. Lighthill [7][8] showed that turbulence in a free field produces a

quadrupole source. Accordingly, the proportionality relationship for the sound power is

$$W \propto U^8 \qquad\qquad 3.3.1$$

where W is the acoustic power of the source and U is the flow rate. The sound power

level can be estimated using,

$$SWL = 10 \log_{10} \frac{C_1 U^8}{W_{ref}} \qquad\qquad 3.3.2$$

where C_1 is an unknown constant and W_{ref} is the reference sound power equal to

$1.0\ pW$.

Curle [10] and Davies and Ffowcs Williams [11] showed that turbulence inside a

pipe produces an acoustic dipole. The source sound power can be expressed using the

proportionality

$$W \propto U^6 \qquad\qquad 3.3.3$$

and the sound power level from turbulence inside of the pipe can be estimated as

$$SWL = 10 \log_{10} \frac{C_2 U^6}{W_{ref}} \qquad\qquad 3.3.4$$

where C_2 is an empirically defined constant.

The constant C_1 and C_2 are frequency dependent and account for the fluid density, dimensions of solid bodies in and around the flow, and the size of the turbulent eddies. By comparing the measurements of the acoustic power of flow noise generated in pipes having different diameters, the dominant source mechanism can be identified. If the measured sound power changes in accordance with one of the proportionalities, it is reasonable to assume that an aeroacoustic source is the dominant source being measured. This comparison method has been developed based on similar comparisons conducted by Kuhn and Morfey [24]. They found that for Mach numbers less than 0.2, the primary source likely results from flow separation in the pipe and is thus defined by the proportionality for a dipole as given in Equation 3.3.4. The jet mixing (a quadrupole source) is then expected to be the dominant source for Mach numbers exceeding 0.2 and thus the sound power will be defined by the proportionality given in Equation 3.3.2

3.3.2 Sound Power Level Vs Frequency

Figure 3-5 shows the initial sound pressure data of the seven microphones for pipe B at flow velocity 0.25 Mach and Pipe C at flow velocity 0.1 Mach. For both pipe sizes, the sound pressure levels at each microphone are similar indicating that the source is roughly omni-directional. The frequency content is broadband except for tones at 120

Hz and 1200 Hz in Figure 3-5a and 1600 Hz in Figure 3-5b. Using Equation 3.1.2 the

sound power is compiled in Figure 3.6 from the measured sound pressure.
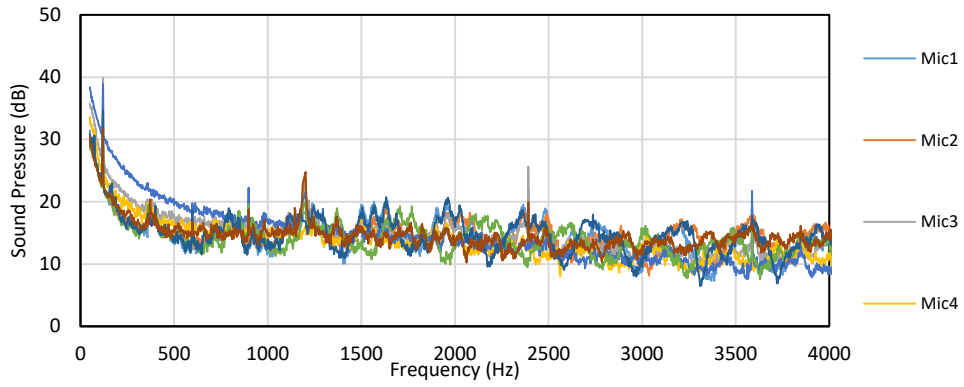
(a)
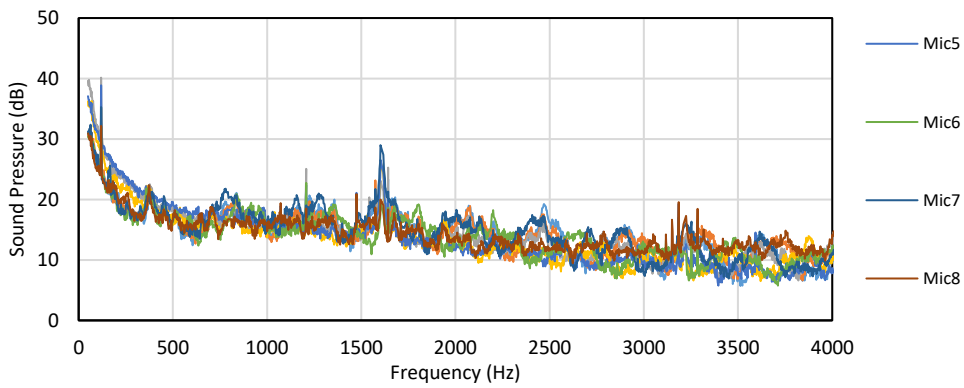
(b)

Figure 3-5 Measured sound pressure of the eight microphones for (a) Pipe B at flow velocity 0.25 Mach and (b) Pipe C at flow velocity 0.15 Mach.
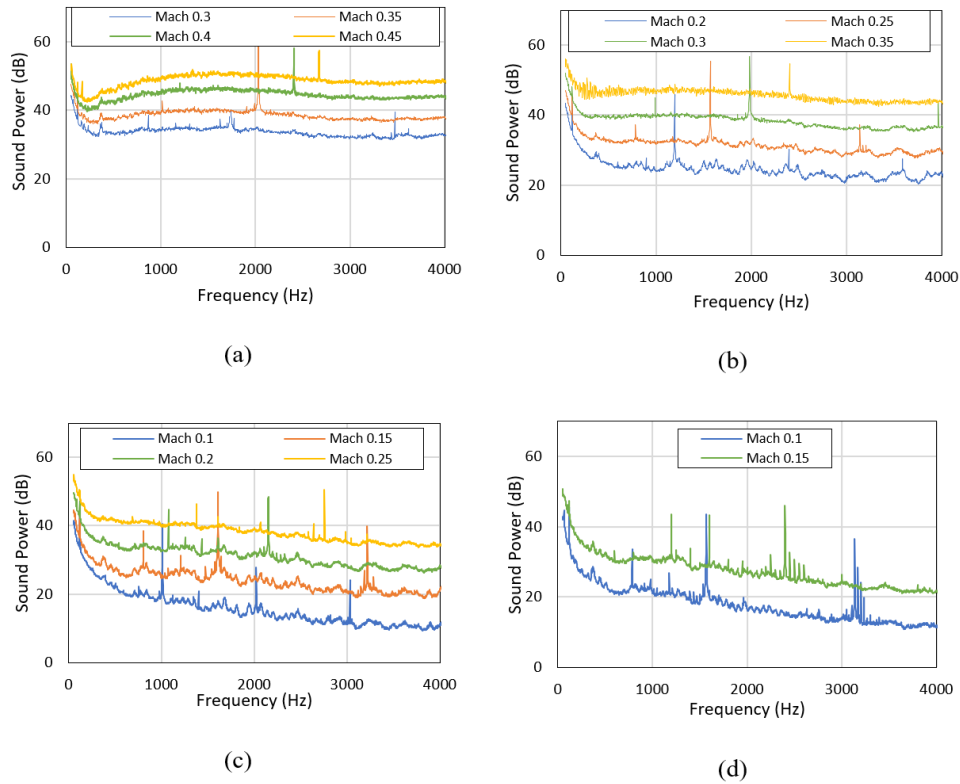
Figure 3-6 Initial results of measuring the sound power of the aeroacoustic noise generated by flow through (a) Pipe A, (b) Pipe B, (c) Pipe C and (d) Pipe D as described in Table 3-1. Note the peaks occurring above 500 Hz.

The peak at 120 Hz is electrical noise due to the blower. The inside of the blower is shown in Figure 3-7. Tones are anticipated at the blade pass frequencies of the blower. The blade pass frequency and its harmonics are defined as

$$BPF_h = h\left(N_b \times \frac{RPM}{60}\right) \qquad 3.3.5$$

where N_b is the number of blades on the fan and h is the order of the harmonic counting 1, 2, 3, ... n. For a flow velocity of 0.4 Mach, the blade pass frequency is approximately 2075 Hz as shown in Figure 3-8. By placing an accelerometer on the blower's fan shroud, it can be observed that the largest acceleration of the shrouds exterior surface correlates

with the spike in the measured sound power and the BPF, as is shown in Figure 3-7. To isolate the flow noise the BPF and electrical noise was filtered out of the data for Pipes A, B, C, and D and then plotted in one-third octave bands in Figures 3-9, 3-10, 3-11, and 3-12.

Figure 3-7 The 48-blade rotor of the regenerative blower used on the muffler test rig.
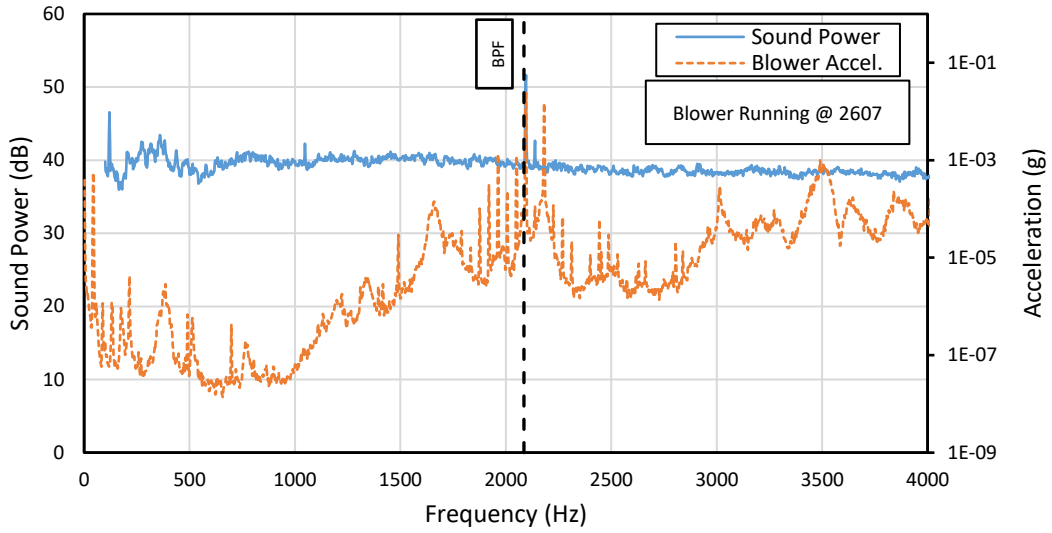
Figure 3-8 Comparison of measured flow noise generated at the end of Pipe A compared to acceleration date collected from exterior surface of the blower's fan shroud. Note the correlation between the peak in the SWL data and the acceleration data at the blower *BPF*.
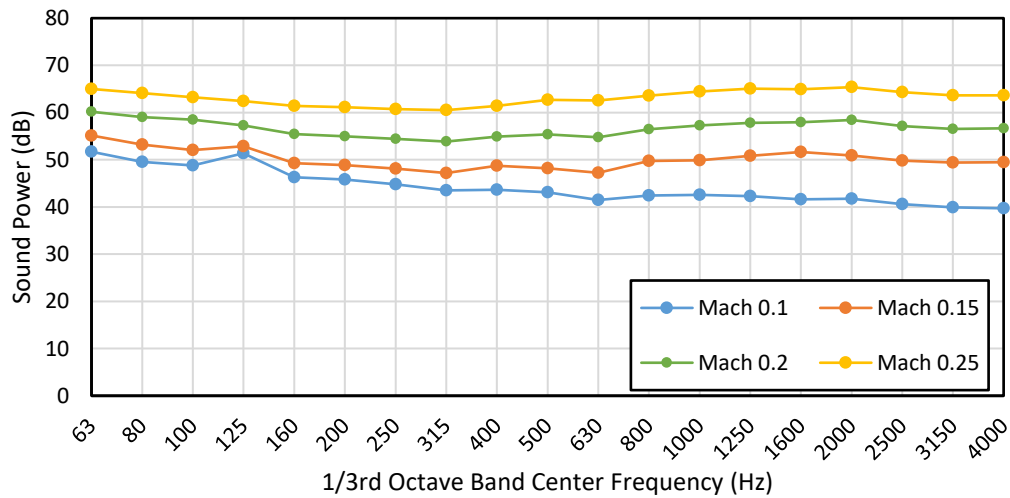
Figure 3-9 The filtered flow noise sound power levels of Pipe A converted into 1/3rd octave bands. With the applied filters the flow noise is fairly broadband.
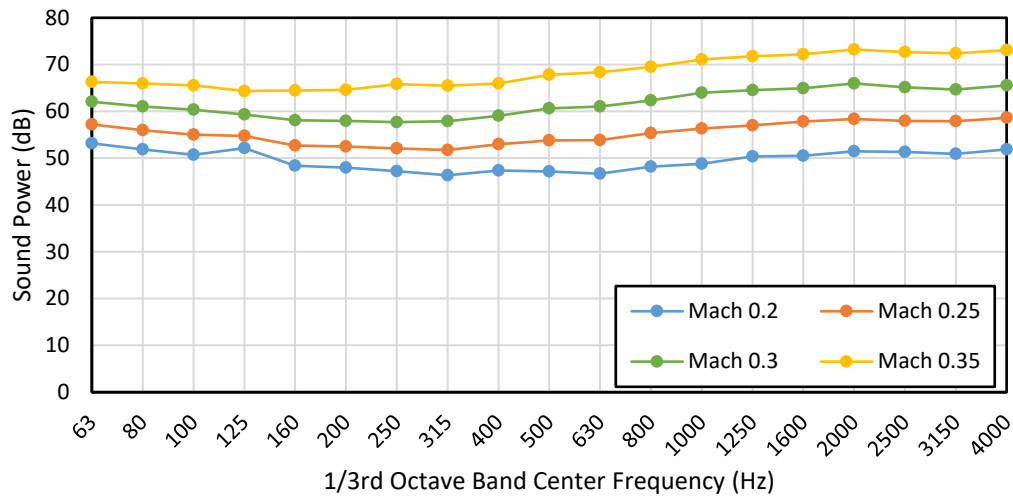
Figure 3-10 The filtered flow noise sound power levels of Pipe B converted into 1/3rd octave bands.
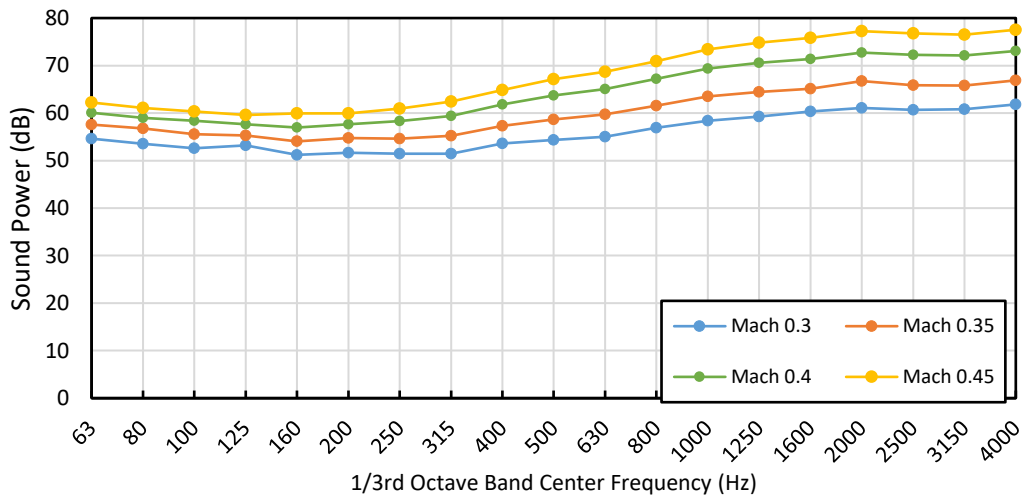
Figure 3-11 The filtered flow noise sound power levels of Pipe C converted into 1/3rd octave bands.
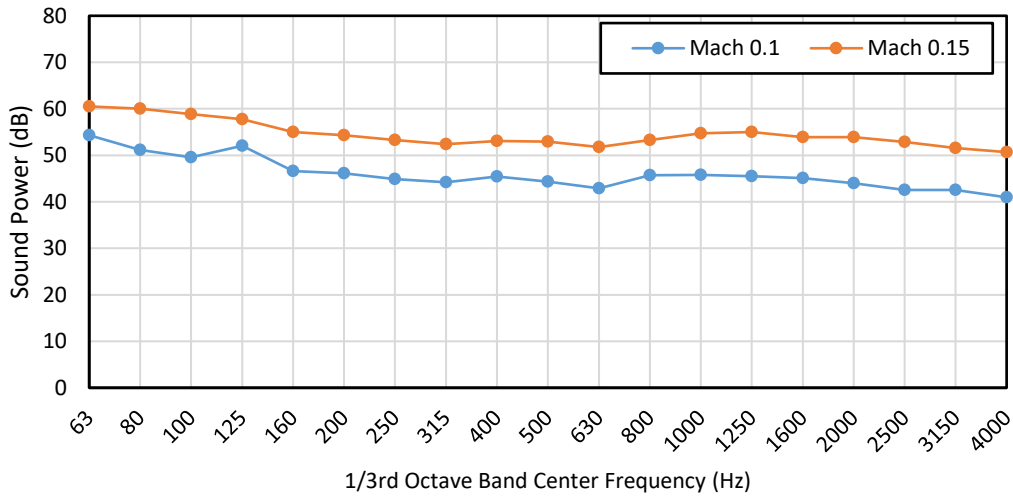
Figure 3-12 The filtered flow noise sound power levels of Pipe D converted into 1/3rd octave bands.

To better understand the results, the sound power level is then plotted as a function of the Strouhal number which is defined as

$$St = \frac{f_c D}{U} \qquad 3.3.6$$

Where f_c is the center frequency of the one-third octave band, D is the inner diameter of the pipe, and U is the flow velocity. As anticipated, the sound power levels increase with increasing flow rates. However, the pipe diameter is inversely proportional to the sound power level for lower Mach numbers (less than 0.25). Figure 3-13 compiles information that may prove useful to industry engineers seeking to qualify their CFD models.
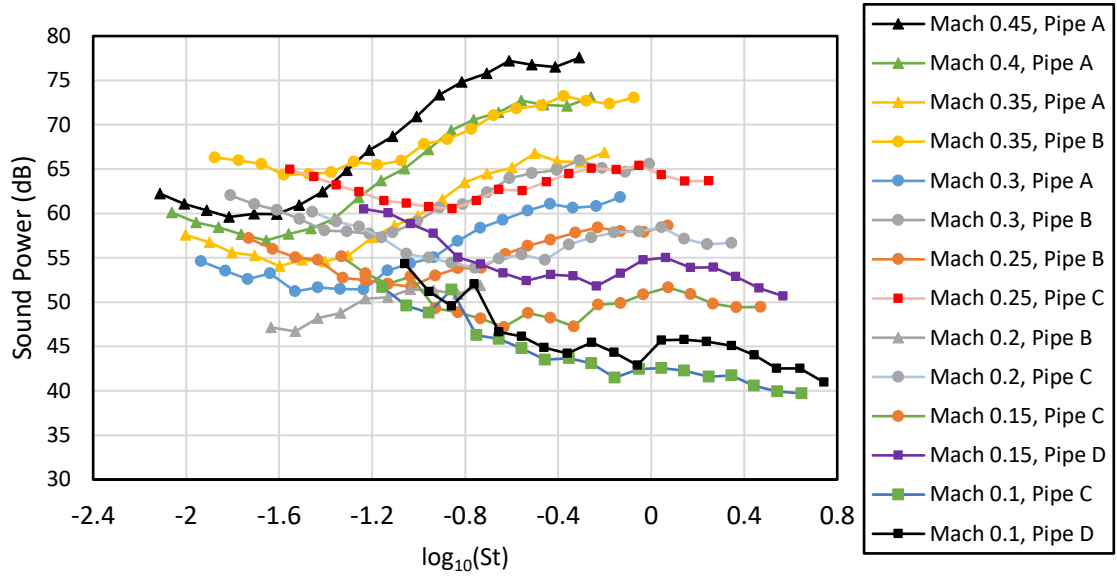
Figure 3-13 Sound power of all 4 pipes as a function of the Strouhal number. Note that as flow velocity increases so does the sound power level. Sound power level is also inversely related to the pipe's diameter for Mach numbers less than 0.3 as can be seen by comparing the levels of Mach 0.25 and Mach 0.2 for pipes B and C or Mach 0.15 for Pipes C and D.

3.3.3   Sound Power Level Versus Mach Number

To validate that flow noise is the dominant source measured the data is compiled in Figure 3-14 with respect to the Mach number and the total sound power of the subsonic jet. By then comparing the rate at which the sound power changes with flow velocity for each pipe to the quadrupole and dipole proportionality, given in Equation 3.3.2 and 3.3.4, a strong correlation between the quadrupole proportionality curve and the sound power at flow rates 0.3 to 0.45 M is observed. In comparison, at the lower flow rates of 0.1 to 0.2 M the change in sound power correlates to the dipole proportionality. These findings imply that turbulence inside the pipe serves as the primary source of noise for Mach numbers less than 0.2. Then for Mach numbers greater than 0.2 the jet mixing region outside the pipe serves as the primary source. These results match the theories of

42

Lighthill, Curle, Davis, and Ffowcs Wiliams which all together demonstrates that there is

no other significant sources contributing to the measured noise other than flow noise.
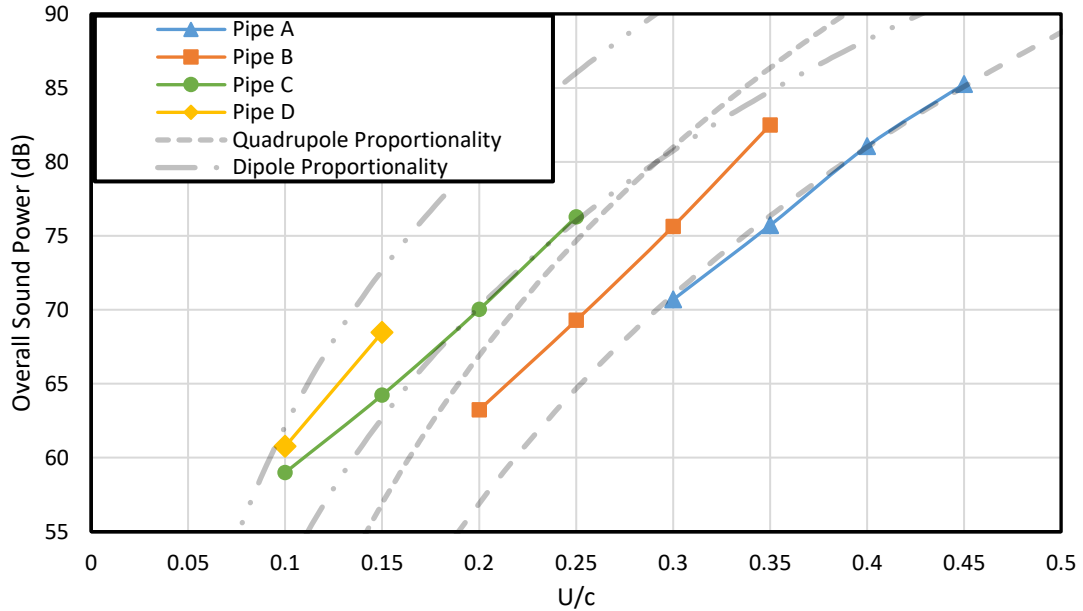
Figure 3-14 The total measured sound power of each pipe with respect to the Mach
number compared to theoretical quadrupole and dipole sources.

3.3.4   Comparison to VDI3733

The German standard VDI 3733 [23] provides acoustic guidance in the planning,

design, and laying of circular cross-sectional pipe in industrial plants. The standard

includes a semiempirical model for predicting internal flow noise for Mach numbers less

than 0.3. The model is based on in-duct measurements of the internal generated flow

noise sound power of straight pipes connected to anechoic terminations. The internal

sound power of the pipe is expressed as

$$W_i = \frac{K_D \rho U^6 S}{c^3}$$
3.3.7

where W_i is the internal acoustic power generated by turbulence inside the pipe, ρ is the density of the fluid, U is the flow velocity, S is the cross-sectional area of the pipe, c is the speed of sound and K_D is a correction factor dependent on the flow velocity. Equation 3.3.7 can be expressed in logarithmic form as

$$L_{W_i} = K + 60 \log_{10} \frac{U}{U_{ref}} + 10 \log_{10} \frac{S}{S_{ref}} + 10 \log_{10} \frac{p}{p_{ref}}$$

$$- 25 \log_{10} \frac{NT}{N_{ref}T_{ref}} - 15 \log_{10} \frac{\gamma}{\gamma_{ref}}$$

<div align="right">3.3.8</div>

where K is a correction factor defined as

$$K = 8 - 0.16U \qquad\qquad 3.3.9$$

and Table 3-2 defines the other variables and reference values.

Table 3-2 Variable Definitions and Reference values used in Equation 3.3.2

Variable	Definition	Reference Value
U	Flow Velocity	$1 \, m/s$
S	Cross-sectional Area	$1 \, m^2$
p	Static Pressure	$101325 \, Pa$
T	Temperature	$273 \, K$
N	Gas Constant	$287 \, J/kg\text{-}K$
γ	Specific Heat Ratio	1.4

For the case of room temperature (20° C) as tested here, the model simplifies to

$$L_{W_i} = K + 60 \log_{10} \frac{U}{U_{ref}} + 10 \log_{10} \frac{S}{S_{ref}} + 10 \log_{10} \frac{p}{p_{ref}} \qquad 3.3.10$$

To convert the total sound power (L_{W_i}) to one-third octave bands, the correction factor $\Delta L_{W,1/3}$ is defined by the standard as

$$\Delta L_{W,^1/_3} = \begin{cases} 5 \quad , \quad \dfrac{f_s}{U} < 12.5 \; m^{-1} \\ 7.23 - 15.5 \log_{10} \dfrac{f_s}{U} \quad , \quad \dfrac{f_s}{U} \geq 12.5 \; m^{-1} \end{cases} \qquad 3.3.11$$

Ducret [25] modified the model in VDI 3733 to predict the radiated sound power from the pipe by assuming the radiated acoustic power of the internal pipe turbulence would be the dominant flow noise source. This assumption has been shown to be valid for Mach numbers less than 0.2 for the pipes considered in this work. To determine the sound power transmitted outside the pipe, the effect of the pipe's termination was accounted for through the application of the reflection coefficient. Thus, the transmitted sound power in decibels is expressed as

$$L_{W_i} = L_{W_i} + \Delta L_{W,^1/_3} + 10 \log_{10}(1 - |R|) - 4.77 \qquad 3.3.6$$

where R is the reflection coefficient at the termination. The reflection coefficient can be estimated neglecting flow using

$$R = 1 + 0.01366ka - 0.59079(ka)^2 + 0.33576(ka)^3$$
$$- 0.06432\,(ka)^4 \qquad 3.3.7$$

where k is the wavenumber and a is the radius of the pipe [26].

The model described above was then used to predict the sound power for lower Mach numbers. Results are shown in Figures 3-15, 3-16 and 3-17. Observe that the agreement is acceptable between prediction and measurement. Surprisingly, the simple model usefully predicted the radiated sound power within 5 dB at most frequencies. These results further demonstrate that the measurements track well with theoretical models and thus, were successfully completed with minimal contamination.
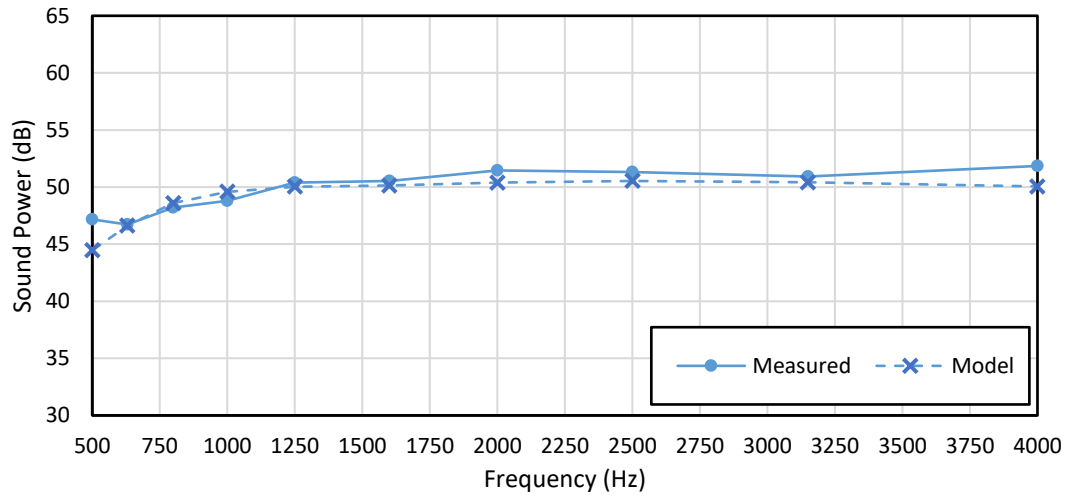
Figure 3-15 Measured sound power in 1/3 octave bands of Pipe B with a flow speed of Mach 0.2 compared to the model predicted sound power.
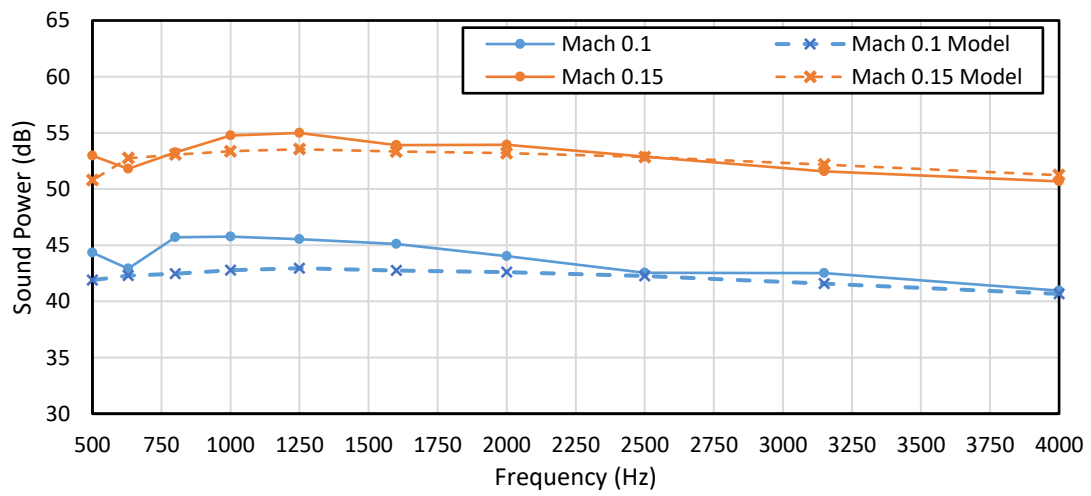
Figure 3-16 Measured sound power in 1/3 octave bands of Pipe C with a flow speed of Mach 0.1, 0.15, and 0.2 compared to the model.
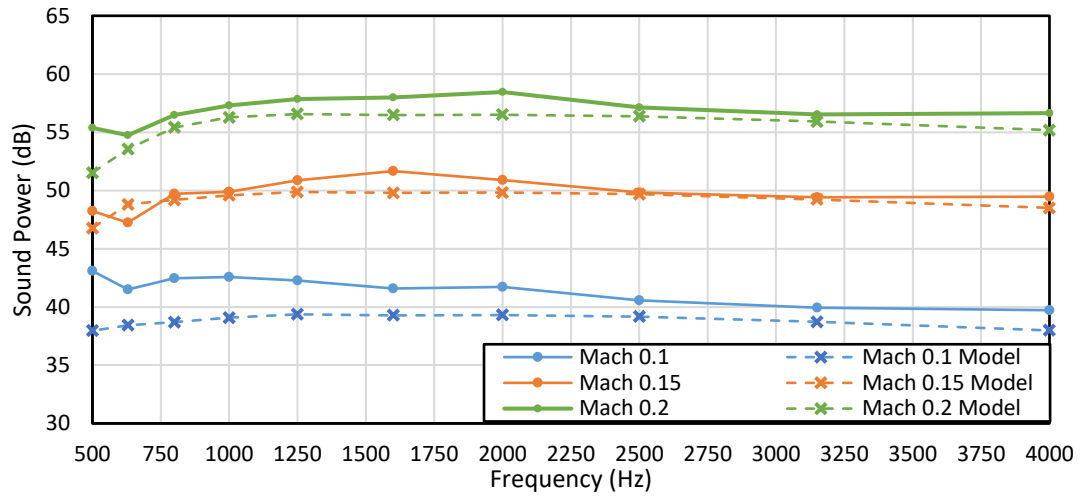
Figure 3-17 The radiated sound power in 1/3 octave bands of Pipe D with a flow speed of Mach 0.1 and 0.15 compared to the model.

3.3.5   Conclusion

In this research, the sound power of a jet at the outlet of pipes with various diameters was measured. By adjusting the flow rate, the different flow regimes, where a dominant dipole or quadrupole source prevailed, were determined. It was observed that the primary source was a dipole for Mach Numbers below 0.2. Considering the pipe diameters in question, this finding aligns with findings from previous historical research. At these lower flow rates, the semi-empirical model from VDI 3733 was successfully employed to accurately predict the sound power radiated from the outlet. These findings suggest that the University of Kentucky's Muffler Flow rig can accurately measure flow noise generated at flow velocities up to 0.2 Mach.

Mach numbers ranging from 0.2 to 0.45 were found to correlate with hypothetical quadrupole sources. These results also align well with past research and demonstrate the capabilities of the flow rig in measuring flow noise up to Mach 0.45. The following

chapter of this work is dedicated to an experimental examination of flow noise generated

by an expansion chamber and a concentric tube resonator using the rig and

methodologies developed here. Chapter 5 then focuses on using the measurement data

collected here to validate a computational aeroacoustics finite element model.

CHAPTER 4. EXPANSION CHAMBER AND CONCENTRIC TUBE RESONATOR CASE STUDY

4.1   Introduction

Several different flow mechanisms can produce noise in mufflers. These sources include jet noise from the tailpipe as was explored in the previous chapter or turbulence inside the muffler. Lighthill [7][8] showed that the sound power of a jet is an ineffective quadrupole source proportional to the velocity of the flow to the eighth power. From the previous chapter, it is reasonable to assume that the jet from the tailpipe of a muffler is a weak source at subsonic flow velocities below 0.2 Mach. Given that, the flow noise from a muffler is expected to be dominated by the internal turbulence of the muffler. This conclusion is best represented in the case of an expansion chamber. Fukuda et. al. [27] investigated flow noise generation from an expansion chamber and determined that the dominant aeroacoustic source is the jet from the inlet pipe hitting the tailpipe opening on the other side of the chamber. This phenomenon was termed jet flow collision. The simplest method for counteracting the extraneous flow noise generated by an expansion chamber was found to be the insertion of a perforated pipe that connects the expansion chamber's inlet and outlet. This configuration is commonly called a concentric tube resonator (CTR). Izumi et. al. [28] demonstrated the effectiveness of this method and compared it to a variety of less effective alterations. It is now commonly accepted that the insertion of a perforated pipe can effectively control the broadband noise generated by jet collision while also improving the muffler's mechanical and acoustic performance. However, perforated pipes can also produce flow generated noise due to other mechanisms.

The flow noise generated by a perforated pipe is a whistle-like tone with frequency and amplitude dependent on the flow velocity, the properties of the perforated pipe, and the cavity/encloser around the pipe. Velocity fluctuations from the turbulent flow passing through the perforate are responsible for the tone generation. Kojima et. al. [29] studied a CTR muffler with an airflow of 50 m/s and found that the whistle noise was related to the velocity fluctuations passing through the first several rows of perforations, the modes of the enclosing cavity and the tailpipe geometry. This correlation suggested a coupling between the flow through the perforations, the muffler chamber, and tailpipe resonances. Yamada et. al. [30] later investigated this relationship by changing the diameter of the encloser around the perforated pipe effectively changing the modes of the enclosing chamber. They noted that the frequency of the whistle noise correlated to the modes dependent on the volume and geometry of the enclosing chamber.

These relationships are further explored in this research. Specifically, the perforation diameter and perforation rate (or porosity) are varied, and the whistle noise and the overall level of flow noise generated in the CTR are investigated.

4.2   Flow Noise Insertion Loss Formulation

To determine the flow noise generated in the perforated pipe CTR, insertion loss is defined in two ways. The first approach is an attempt to isolate the flow noise generated by the outlet jet from noise generated by the muffler. This will be referred to as the flow noise insertion loss of the muffler $\left(IL_{muffler}^{flow}\right)$ and is defined as

$$IL_{muffler}^{flow}(U_0) = SWL_{flow}^0(U_0) - SWL_{flow}^1(U_0) \qquad\qquad 4.2.1$$

where SWL_{flow}^0 is the sound power at the outlet of a straight pipe with a mean flow

velocity U_0 and SWL_{flow}^1 is the sound power at the outlet of the test muffler at a flow

velocity U_0. The straight pipe reference for $IL_{muffler}^{flow}$ has the same length as the test

muffler and the same inner diameter as the outlet of the test muffler.

The second approach is an experimental attempt to isolate the flow noise

generated by a single component of the muffler from the rest of the muffler and is

referred to as the flow noise insertion loss of a component $\left(IL_{comp.}^{flow}\right)$. It is defined as the

difference between the flow noise at the outlet of the system with $\left(SWL_{flow}^w\right)$ and

without $(SWL_{flow}^{w/o})$ the component. $IL_{comp.}^{flow}$ is calculated using

$$IL_{comp.}^{flow}(U_0) = SWL_{flow}^{w/o}(U_0) - SWL_{flow}^w(U_0) \qquad\qquad 4.2.2$$

where $SWL_{flow}^{w/o}$ is the sound power of the expansion chamber with no perforated pipe

insert, and SWL_{flow}^w is the flow noise generated at the muffler's outlet with a perforated

pipe installed.

4.3　Test Cases

A total of eight cases were considered and are listed in Table 4-1. A straight pipe

and the muffler with no inserted perforated pipe were measured to establish reference

levels for insertion loss determination. An image of the straight pipe and the muffler are

shown in Figure 4-1a. Figure 4-1b provides the dimensions of the muffler.

Table 4-1 The dimensions and names of the eight measured cases.

Case Name	Hole Pattern	Hole Diameter (d_h) (mm)	Grid Spacing (d) (mm)	$O.A.$ (%)
Straight Pipe	N/A	N/A	N/A	N/A
Expansion Chamber	N/A	N/A	N/A	N/A
Perf 1	Square	4.7	17.2	6
Perf 2	Square	3.2	20.2	2
Perf 3	Square	3	9.5	8
Perf 4	Square	3	6	20
Perf 5	Square	3.5	4.6	45
Perf 6	Hexagonal	0.8	4.2	3

(a)

(b)
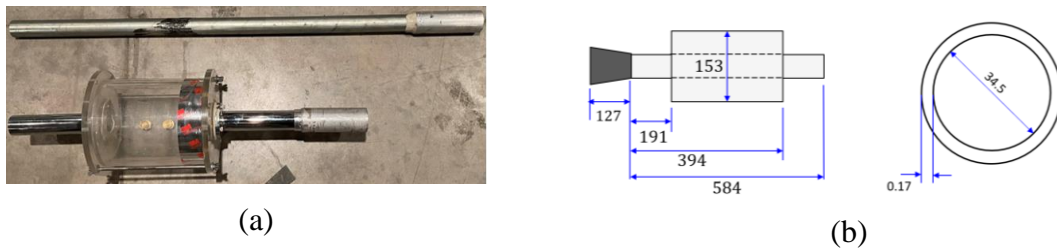
Figure 4-1 (a) The straight pipe and muffler used in this work. (b) Schematic of the muffler with dimensions in mm. The conical adaptors used to connect the straight pipe and muffler to the flow rig are a 47.5 mm to a 34.5 mm diameter.

The six perforated pipes are shown in Figure 4-2. Figure 4-3 gives the pressure drop of each of the CTR and the expansion chamber mufflers. Each test case was measured at ten flow velocities ranging from 0.1 to 0.28 Mach with a 0.02 Mach increment. Due to the nature of the rig, it is difficult to precisely measure the flow velocity. To account for this variability, all measurements were performed twice. Repeating the measurements twice also allowed for a check on the repeatability of the whistle noise and the flow noise insertion loss calculations.
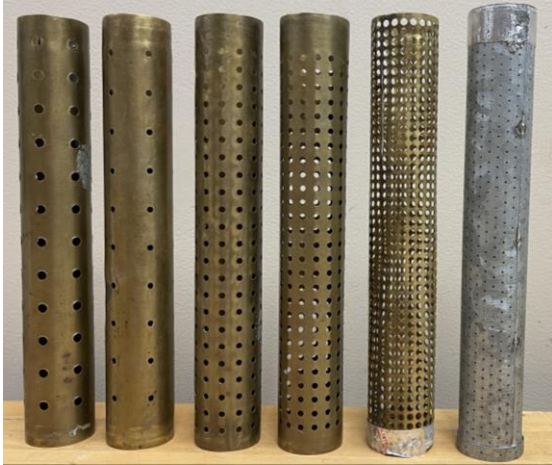
Figure 4-2 An image of the six perforated pipes lined up in numerical order from left to right.
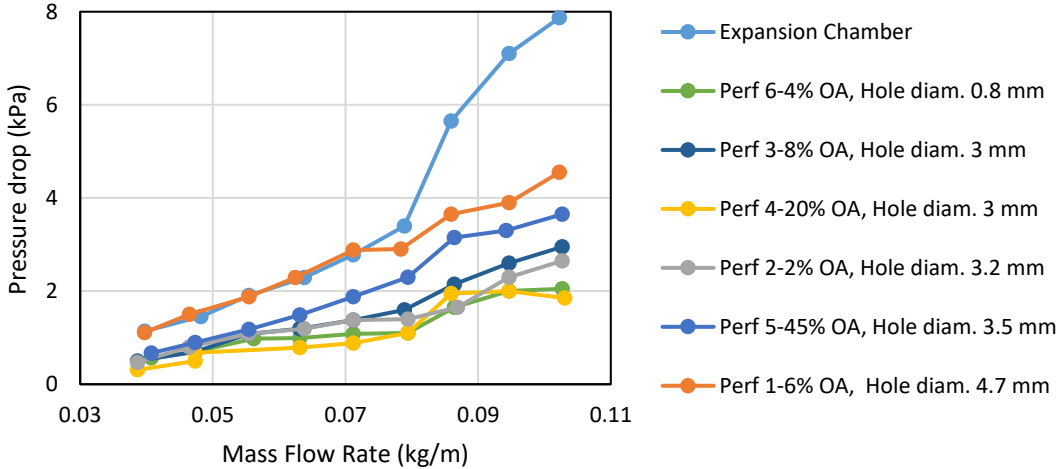
Figure 4-3 The pressure drop of the expansion chamber and the 6 CTRs created by the perforated pipes.

4.4   Characteristics of the Flow Generated Noise

The relationship between the sound power level (SWL), the flow noise spectrum, and the flow velocity was examined for all test cases in Figure 4-4. As discussed earlier, the flow generated noise from the straight pipe is broadband and primarily due to

turbulence inside the pipe and the subsonic jet at the outlet. Any variation from this

suggests that a new aeroacoustic source is present. For example, the expansion chamber

increases the generated broadband noise and obvious tones are noted at 800 Hz, 900 Hz,

1.6 kHz, and 2.2 kHz.
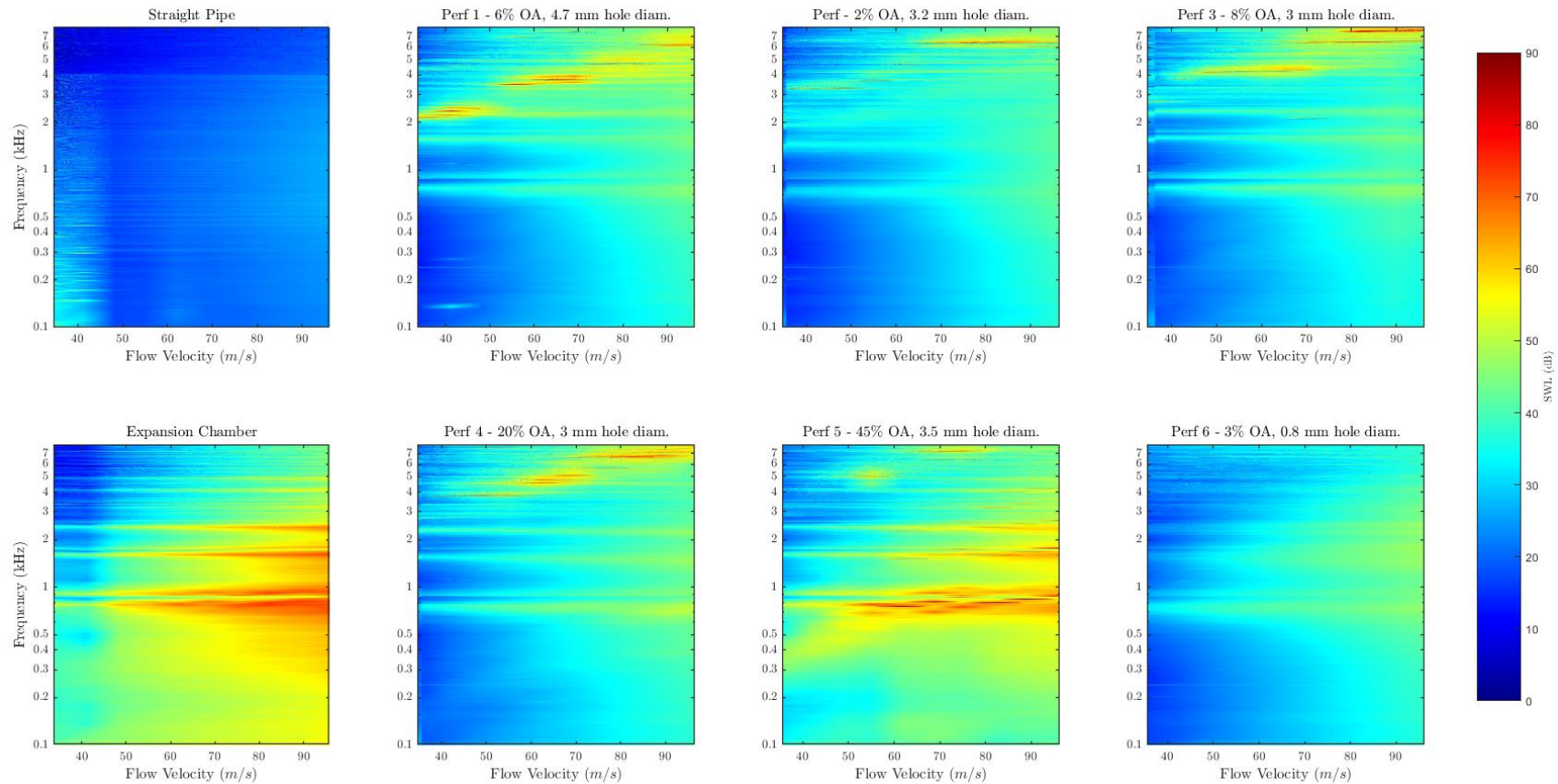
Figure 4-4 Broadband sound power spectrum of the 8 test cases with respect to the flow velocity. Note the primary excited frequencies of the expansion chamber are present in all perforated tube cases. The excited whistle frequency of the perforated tubes corresponds to an excited frequency of the expansion chamber and increases in frequency with the flow velocity.

Considering the perforated pipe cases, the generated whistle noise is manifested as an obvious tone. This tone increases in frequency with the flow velocity. For example, in the case of Perf 1, the dominant sources are between 2 and 3 kHz at velocities less 50 m/s, and between 3 and 4 kHz at flow velocities between 60 and 70 m/s. These tones are produced in the expansion chamber and are manifested as a whistle noise. This relationship can be seen in all the perforated pipe-cases but is most prominent for Perf 5. From Figure 4-4, it can be concluded that the frequency of the whistle noise is inversely proportional to the diameter of the hole, is proportional to the mean average flow velocity and correlated to the expansion chamber's geometry. These conclusions are like those of Kojima et. al. [29] and Yamada et. al. [30].

4.4.1   Strouhal Number of the Whistle Noise

The Strouhal Number (St) is a nondimensionalized frequency that is often used to describe flow noise and is particularly useful when considering frequency dependent phenomena. As the frequency of the measured flow noise corresponds to the frequency of the vortex shedding of an aeroacoustic source, the Strouhal number for a perforated pipe is defined as

$$St = \frac{f\,d_h}{U_0} \qquad\qquad 4.2.2$$

where f is the frequency, d_h is the perforation diameter, and U_0 is the flow velocity. Figure 4-5 shows the relationship between the Strouhal number, the flow velocity, and the SWL of the generated flow noise for the six perforated pipes. The high sound power at the whistle tones is easily seen. For Perfs 1, 2, 3, and 4, the whistle noise is generated at Strouhal numbers between 0.2 and 0.35.

56
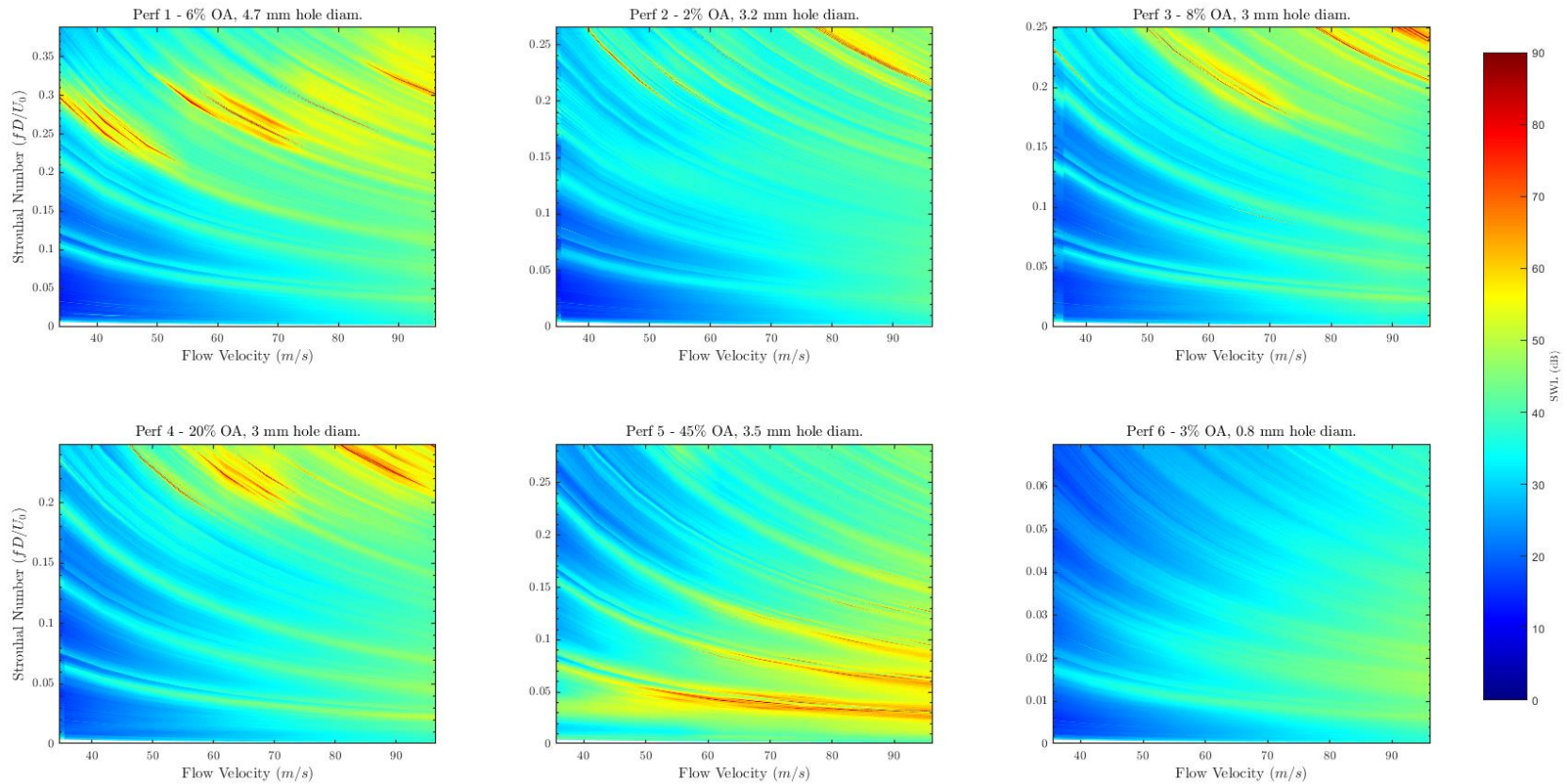
Figure 4-5 The Strouhal frequency of the 6 perforated tube plotted with respect to the flow velocity and sound power. Note the no matter the perforated tube the same bands are excited. These   excited bands are controlled by the modes of the expansion chamber, while a peak or "whistle" occurs in one of these modes, which is controlled by the perforated tube.

As the $O.A.$ increases, so does the range of Strouhal numbers for which the whistle noise is generated at a particular flow velocity. This is apparent when comparing Perf 3 and 4 at flow velocities between 60 and 70 m/s. For Perf 3, the whistle noise is generated for Strouhal numbers between 0.2 and 0.22. For Perf 4, which has a substantially large $O.A.$, the high whistle noise is evident across Strouhal numbers ranging from 0.2 to 0.25. Since the diameter of the perforation and flow velocities are held constant between Perf 3 and 4 the increased range of excited Strouhal numbers must correspond to an increased range of frequencies at which vortex shedding is occurring. The increased range of excited frequency content corresponds to a 5 dB increase in the overall SWL. This increase in strength agrees with the findings of Kojima et. al. [29] who concluded that the first couple of rows of perforates were the main source of the whistle noise. An increase in the open area ($O.A.$) leads to more rows in the initial length of the perforated section contributing to the flow noise generation which is manifested in the whistle noise. As the rate of vortex shedding does not necessarily occur at the same rate within each row or perforation, this, in turn, leads to a greater number of excited frequencies and an overall increase in Sound Power Level (SWL) of the generated flow noise.

4.4.2 Repeatability of Generating the Whistle Noise

The repeatability of the generated whistle noise was checked for all cases. Figures 4-6, 4-7, and 4-8 show a comparison of the measured narrowband content for Perf 1, 2 and 3. From these plots it was determined that under the same flow conditions, the generation of the whistle noise was repeatable within about 10 Hz. It is likely that the amplitude of the tone varied between tests, due to minor variations in the flow conditions.
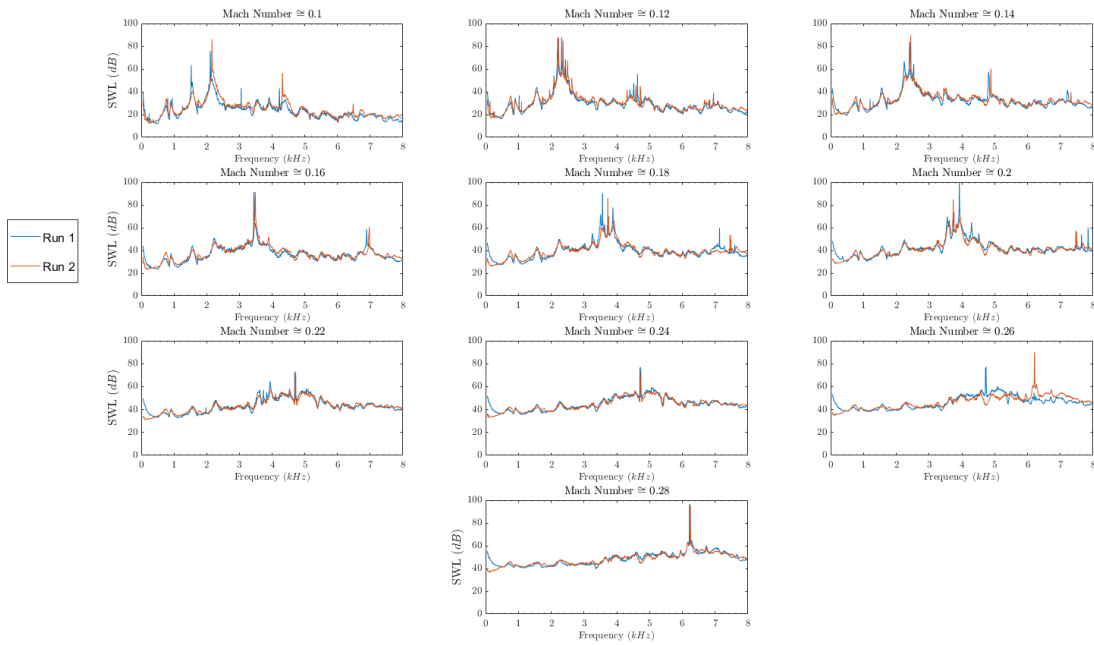
Figure 4-6 The sound power spectrum of perforate tube 1 for two completed measurements.
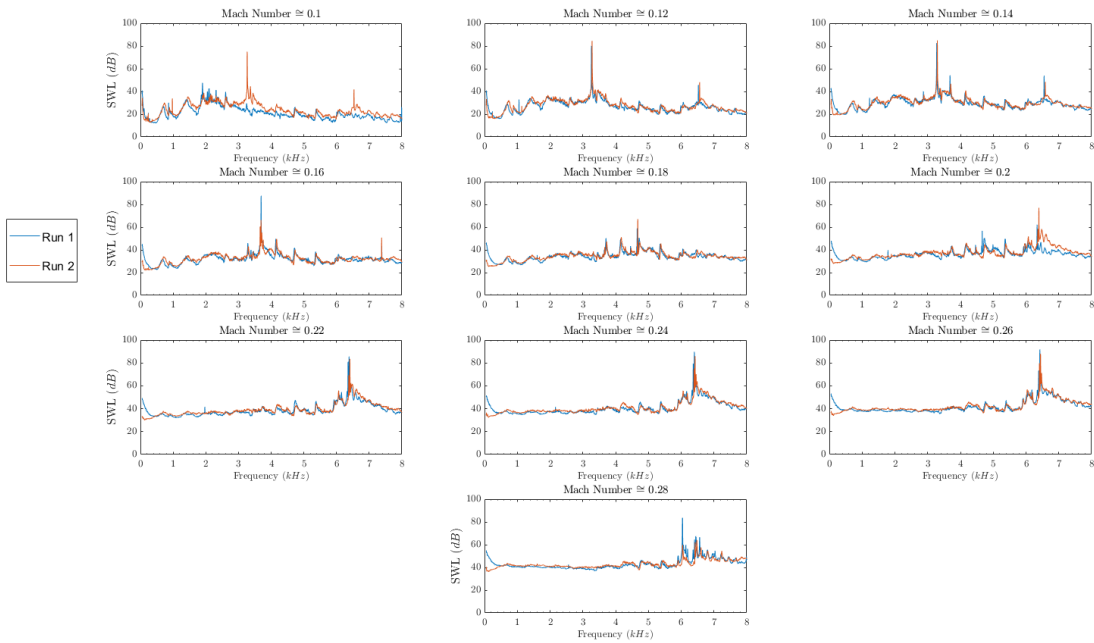
Figure 4-7 The sound power spectrum of perforate tube 2 for two completed measurements.
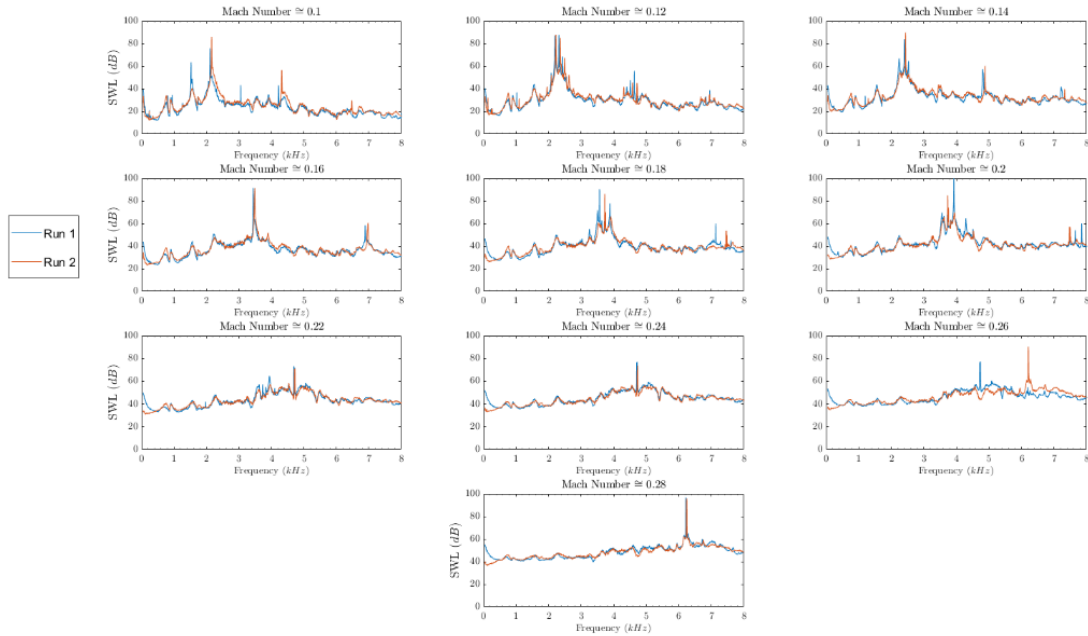
Figure 4-8 The sound power spectrum of perforate tube 4 for two completed measurements.

4.5 Flow Noise Insertion Loss

The increase in the SWL of the generated flow noise from the expansion chamber and the perforated pipes was determined using the flow noise insertion loss methods in Equations 4.2.1 and 4.2.2. The insertion loss of each case was calculated in terms of one-third octave bands. When considering these results, recall that the insertion loss is the difference between the sound powers. Hence, a positive value indicates a decrease in the SWL whereas a negative value indicates an increase in the SWL.

4.5.1 Flow Noise Insertion Loss of the Muffler

The flow noise insertion loss of the expansion chamber and the perforated tube CTRs using Equation 4.2.1 are plotted in Figures 4-9 and 4-10, respectively. The results are plotted with respect to the one-third octave band center frequency and the flow

60

velocity. For Figures 4-9 and 4-10, the range for the insertion loss is limited to ± 20 dB though values of the insertion loss range between ± 40 dB.
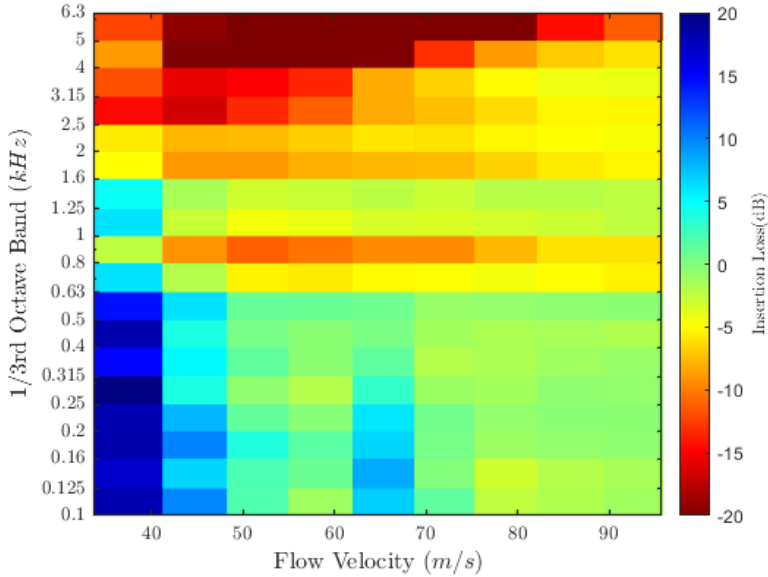
Figure 4-9 The flow noise insertion loss of the expansion chamber as defined by Equation 4.2.1 and with respect to the flow velocity.

The expansion chamber increases the SWL by approximately 10 dB at flow velocities greater than 45 m/s (0.13 Mach). This gain in SWL is due to the jet stream collision and shows up at frequencies of 0.8 to 1 kHz and 2 kHz and up. The jet stream collision generates flow noise at frequencies that depend on the dimensions of the expansion chamber as discussed in Fukuda et. al. [27]. In addition, there is a reduction in the flow generated noise below 0.63 kHz for flow velocities below 45 m/s (0.13 Mach). At low velocities, insufficient energy is present at the inlet of the expansion chamber for the jet to collide with the outlet with significant enough force to create the eddies necessary for the generation of flow noise at the low frequencies below the 0.63 kHz band. Additionally, due to the pressure drop across the muffler, the outlet jet stream is at a lower velocity than the straight pipe case, and thus the overall SWL of the generated

noise decreases. However, the SWL increases at all measured flow velocities between the 0.8 and 1 kHz bands, as this likely marks a mode of the expansion chamber.

The perforated tube CTR configurations of Perf 1, 2, 3, 4, and 6 exhibit similar behavior to the expansion chamber, as shown in Figure 4-10. These five CTRs increase the SWL in between the 0.8 to 1 kHz bands, further suggesting that there is a mode of the expansion chamber in this frequency range. Comparing Perf 3 and 4, it is observed that the SWL of this excited mode is heightened as the $O.A.$ of the perforated tube is increased. Above 2 kHz, the whistle noise increases the SWL significantly in all six cases. Perf 5, which has the largest $O.A.$ of the six cases, caused an increase in SWL from 10 to 20 dB for flow velocities above 40 m/s. At lower flow velocities, the gain is from 0 to 5 dB. From the comparison of Perf 3 and 4 and the results of Perf 5, it can again be concluded that a larger $O.A.$ may increase the SWL of the flow noise.
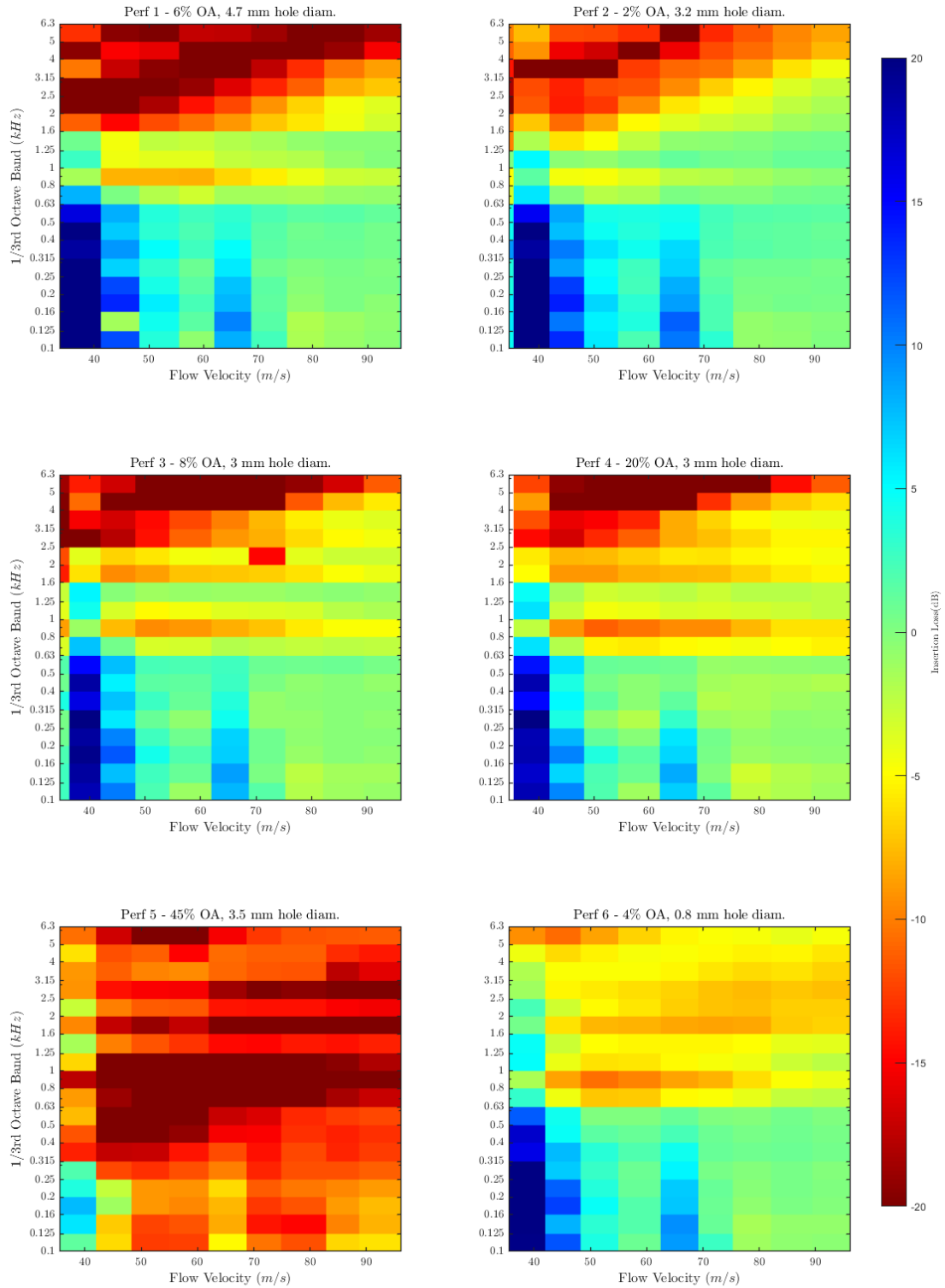
Figure 4-10 The flow noise insertion loss of the six CTR muffler as defined in Equation 4.2.1 with respect to the flow velocity.

4.5.2 Flow Noise Insertion Loss of a Component

The flow noise insertion loss of a component was determined for the six perforated pipes using Equation 4.2.2. The results are plotted versus the flow velocity in Figure 4-11. For Perf 1, 2, 3, 4, and 6, the SWL of the flow noise decreases by 30 to 40 dB below 1.25 kHz. The whistling noise generated by the perforated tube increases the SWL by about 20 dB above 2 kHz for flow velocities less than 50 m/s. As the flow velocity increases, the whistle noise is observed at higher frequencies. Perf 5 is the only case in which the SWL of the flow-generated noise is either greater than or equivalent to the SWL of the expansion chamber. This variance in Perf 5 is likely due to its substantially larger $O.A.$ compared to the other five perforated tubes. Considering all six perforated pipes, it can be concluded that minimizing the hole diameter and the $O.A.$ will maximize the effectiveness of the perforated pipe in controlling the jet collision noise.
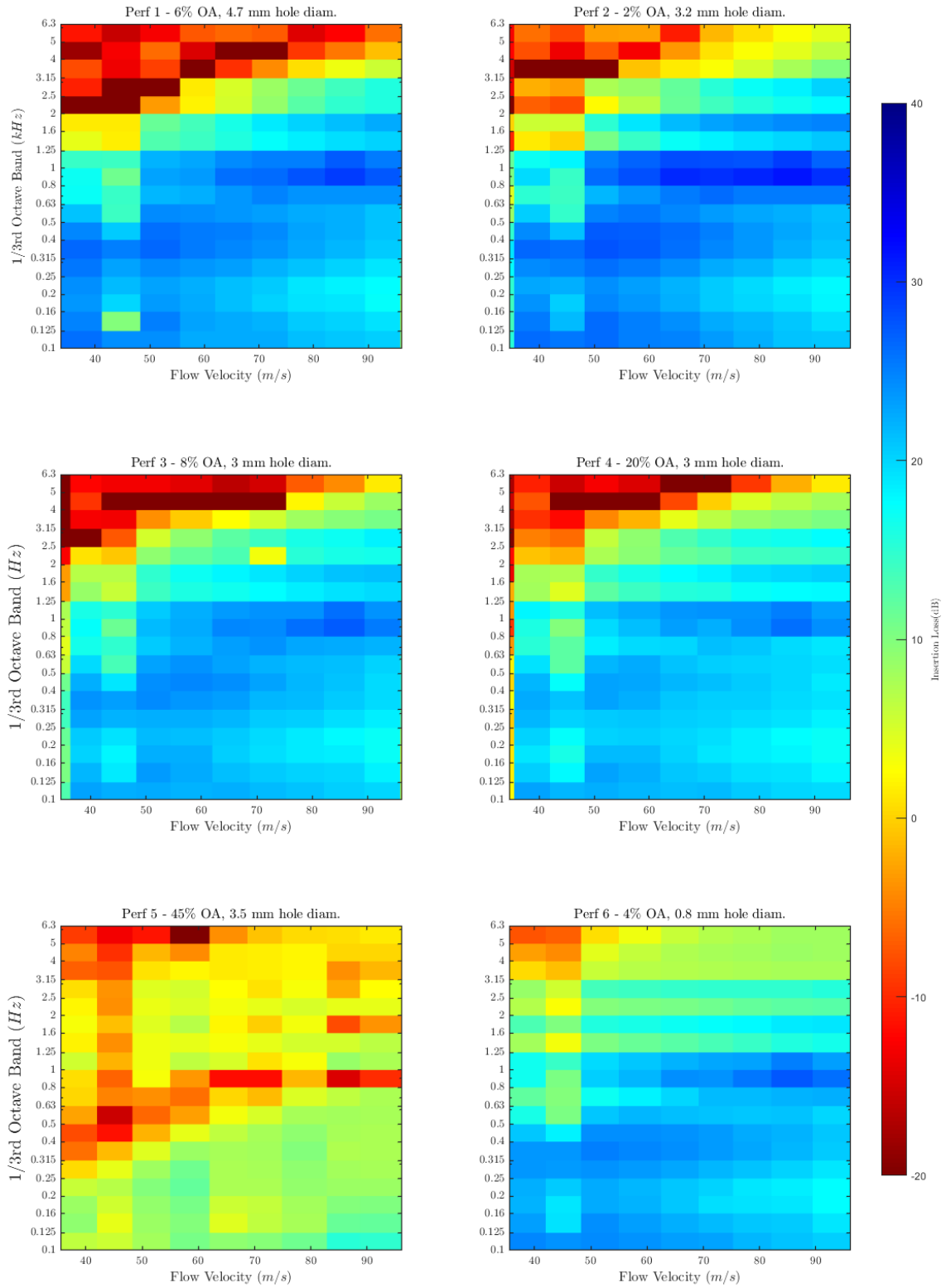
Figure 4-11 The flow noise insertion loss of the six perforated pipes as defined by Equation 4.2.2 and with respect to the flow velocity.

4.5.3 Repeatability of Flow Noise Insertion Loss

Figure 4-12 compares the measured flow noise insertion loss of Perf 1 across two separate completed measurements. Across the ten flow velocities, only the amplitude of the flow noise insertion loss of a component significantly varied for each case. The flow noise insertion loss can thus be repeated for frequency, but the amplitude will vary within a couple of decibels due to variations in the flow conditions between the reference and measured case.
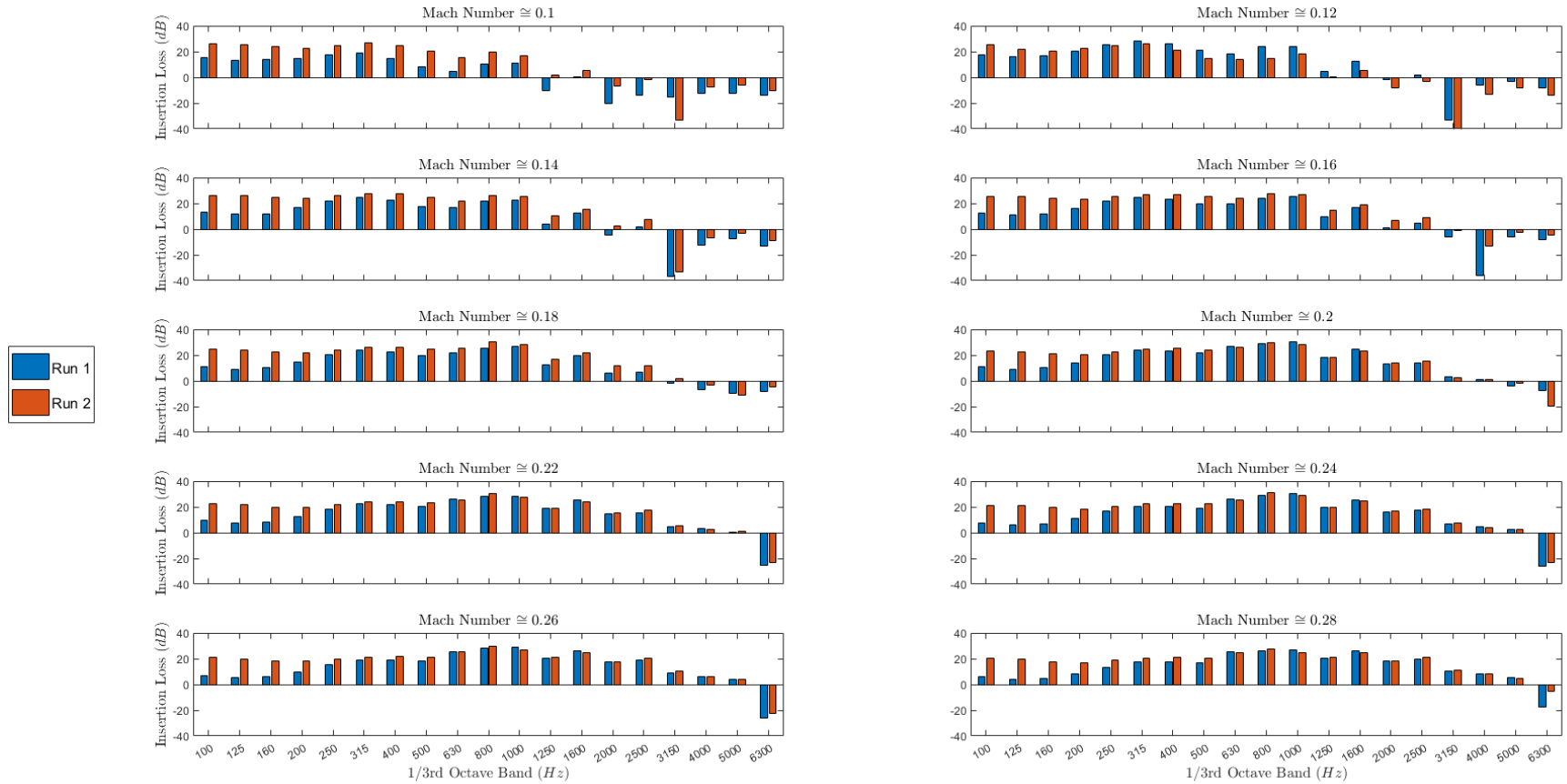
Figure 4-12 Comparison of the calculated 1/3rd octave flow noise insertion loss of perforated tube 1 after two completed measurement runs.

4.6   Conclusion

A measurement campaign has been performed to determine the flow noise from concentric tube resonators with a perforated pipe connecting the inlet to the outlet. The flow rig setup at the University of Kentucky is ideal for determining the flow generated noise inside the muffler because the blower noise is attenuated. In practice, flow noise may be considered inconsequential so long as the noise from the source overpowers that from the flow. However, the results presented here demonstrate that the flow noise can be significant and is tonal in nature. If this noise is not masked, it likely must be addressed.

Several conclusions can be made. First, the frequency of the whistle noise generated by a perforated pipe inside a CTR is proportional to the flow velocity and inversely proportional to the hole diameter of the perforations. Hence, the frequency of the whistle is controllable. Secondly, the amplitude of the whistle noise increases with the open area of the perforated pipe. This increase in amplitude is likely due to an increased number of perforations contributing to the noise. Hence, it is best to minimize the perforation rate. Finally, minimizing the percentage of open area and the hole diameter of the perforations reduces the generated flow noise. However, doing so may also reduce the effectiveness of the muffler for attenuating source noise. Thus, designers will likely need to find a balance between controlling flow noise generation in the muffler and maximizing the muffler effectiveness.

CHAPTER 5. COMPUTATIONAL AEROACOUSTICS APPROACH

5.1   Introduction

Computational aeroacoustics (CAA) is designed to analyze the generation of noise from turbulent flow through the application of numerical methods. With recent advancements in computational power, CAA has become more widely accessible. There are two primary approaches to CAA: the direct method and the hybrid method. The direct method employs Computational Fluid Dynamics (CFD) code to compute an acoustic solution directly. Conversely, the hybrid approach utilizes a solution obtained from a CFD code to formulate acoustic sources. These acoustic sources are subsequently employed as inputs into a dedicated finite element acoustic code to estimate noise generation and acoustic propagation.

Direct methods are more computational expensive than hybrid methods, as they require a transient compressible CFD solution and a very fine mesh to capture acoustic propagation. Typically, a specialized solver is required as most commercial CFD codes are not suitable for developing an acoustic solution. CFD solutions are traditionally solved in the time-domain making it difficult to capture frequency dependent aeroacoustic phenomena. Additionally, the boundary conditions used in CFD solvers are not appropriate for acoustic domains. For example, pressure equal to zero at a boundary in a CFD solver equates to an outlet while in an acoustic domain this equates to a reflective surface. Due to the increased complexity and the high computational cost, direct methods are not particularly applicable for the intensive fast-paced use of industry.

Hybrid methods decouple the flow and acoustic fields by assuming a one-way interaction from the flow field on to the acoustic field. By decoupling the flow and acoustic fields, the transient CFD and acoustic solution are independently determined using commercially available CFD and acoustic codes respectively. The significant advantage of employing hybrid methods lies in the substantial reduction of computational costs. Moreover, the boundary conditions within the acoustic domain are well-suited for the accurate computation of acoustic propagation. These advantages render hybrid methods particularly suitable for widespread application in industry.

However, a notable limitation of hybrid methods is their dependence on the ability to decouple the acoustic and flow fields into a one-way interaction. While this assumption holds true in many scenarios, it is not universally applicable, as exemplified by cases such as the generation of whistle noise through flow in a concentric tube or Helmholtz resonator.

This work demonstrates the capabilities of CAA hybrid methods in the prediction of aeroacoustic phenomena and describes the methodology used in the construction of a model. The CAA model constructed here attempts to predict the noise generated from a subsonic jet at the outlet of a straight pipe. The pipe has an outer diameter of 1.625 inches ($41.3\ mm$) and a wall thickness of 0.13 inches ($3.3\ mm$). The flow through the pipe generating the jet has a flow velocity of $\sim 32\ m/s$. The solution of the CAA model is validated using the measured sound power at the outlet of such a pipe connected to University of Kentucky's muffler flow rig.

The flow field is determined using the commercially available CFD solver scFLOW from MSC Software. The acoustic sources and propagation are solved for using

the commercially available acoustic finite element software Actran also from MSC

Software. The model will be constructed following the procedure outlined in the flow

chart presented in Figure 5-1. The subsequent section provides a detailed breakdown of

the methodology utilized in the development of both the CFD and acoustic models. The

simulation results are then compared to the measured data, and an investigation into the

impact of the truncation filter on the accuracy of the model's solution is conducted.
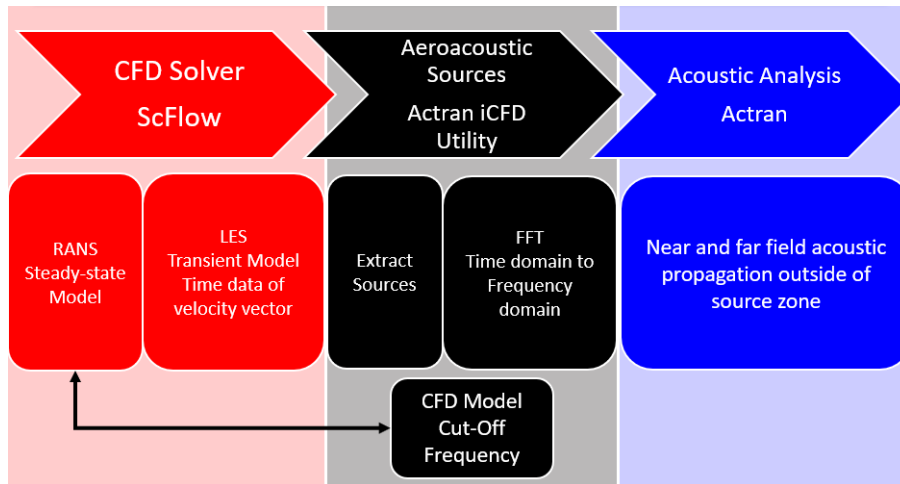
Figure 5-1 Diagram of the workflow used to construct the CAA hybrid model of this work.

5.2   Background

Hybrid methods depend on the utilization of Lighthill's Analogy to extract

aeroacoustic sources from a transient CFD solution. Subsequently, these extracted

sources are mapped onto an acoustic mesh to drive an acoustic solution. The

commercially available acoustic finite element solver, Actran, incorporates a built-in

iCFD utility for extracting aeroacoustic sources from a provided transient CFD solution

using Lighthill's Analogy.

71

5.2.1 Application of Lighthill's Analogy in a Finite Element Code

Lighthill's equation can be converted into the frequency domain as given in Equation 2.2.7. These sources can be included in the finite element formulation by multiplying then by the shape function (Na) and taking the volume integral. This results in,

$$-\omega^2 \int_V N_a \rho_0 dV - \int_V \frac{\delta}{\delta x_i}\left(N_a c_0^2 \frac{\delta \rho_0}{\delta x_i}\right) dV + \int_V \frac{\delta N_a}{\delta x_i} c_0^2 \frac{\delta \rho_0}{\delta x_i} dV$$
$$= \int_V \frac{\delta}{\delta x_i}\left(N_a \frac{\delta T_{ij}}{\delta x_i}\right) dV - \int_V \frac{\delta N_a}{\delta x_i} \frac{\delta T_{ij}}{\delta x_i} dV$$

$$\text{5.2.1}$$

According to Gauss Theorem,

$$\int_V \frac{\delta F_i}{\delta x_i} dV = \oint_S F_i n_i dS \qquad \text{5.2.2}$$

is true, thus the finite element formulation of Lighthill's equation is recast as

$$\omega^2 \int_V N_a \rho_0 \, dV - \int_V \frac{\delta N_a}{\delta x_i} c_0^2 \frac{\delta \rho_0}{\delta x_i} dV$$
$$= i\omega \oint_S N_a \rho_0 v_i n_i \, dS + \int_V \frac{\delta N_a}{\delta x_i} \frac{\delta T_{ij}}{\delta x_j} \, dV$$

$$\text{5.2.3}$$

The two terms on the right-hand side of Equation 5.2.3 define two types of acoustic sources. The first term defines a Lighthill surface source. Surface sources are applicable in case of flow fluctuations across a boundary. A common application of such a source is the boundary of rotating equipment such as a fan or rotor. The second term on the right-hand side represents a Lighthill volume source. Lighthill volume sources model vortex shedding such as occurs inside a pipe or a turbulent jet.

As the model in this work will not include the flow source, a regenerative blower,

Equation 5.2.3 simplifies to

$$\omega^2 \int_V N_a \rho_0 \, dV - \int_V \frac{\delta N_a}{\delta x_i} c_0^2 \frac{\delta \rho_0}{\delta x_i} dV = \int_V \frac{\delta N_a}{\delta x_i} \frac{\delta T_{ij}}{\delta x_j} \, dV \qquad \qquad 5.2.4$$

To complete the extraction and formulation of the aeroacoustic sources the, Actran iCFD

utility uses the CFD results and Equation 5.2.4.

5.2.2   Computational Fluid Dynamics (CFD) Turbulence Models

Eddies in turbulent flow manifest in various sizes, stimulating momentum

exchange and influencing the velocity distribution of the flow. To achieve accurate

numerical analysis of the flow, it is essential to capture these eddies and their effects.

Given that turbulent flow comprises numerous eddies and vortices, directly simulating

them using current computational resources is impractical. Consequently, CFD models

leverage turbulent models, as discussed in Section 2.3, to mitigate the computational cost

of simulating turbulent flow. In this study, both steady-state and transient CFD models

are constructed. The steady-state model involves a Reynolds Averaged Navier-Stokes

(RANS) simulation utilizing the SST $k - \omega$ turbulence model. On the other hand, the

transient model employs Large-Scale Eddy Simulation (LES).

The RANS CFD method averages turbulent flow over a period of time to derive a

time-averaged steady-state solution. The influence of turbulence is considered by solving

for the eddy viscosity through the application of a turbulence model. Turbulence models

disregard small eddies which substantially decreases the number of necessary mesh

elements. As a result, RANS models have reduced computational costs in comparison to other methods.

In this work the shear stress transport (SST) $k - \omega$ turbulence model as defined by Menter [20] and implemented in scFLOW is used. The SST $k - \omega$ model was chosen for its improved approximation of near-wall turbulence without the need for additional damping functions. This decreases the total computational power needed and time to solve within the region of pipe flow. Secondly, the SST $k - \omega$ model is known to produce a better estimate of boundary layer separation, such as will occur at the pipe's exit. Finally, using the SST $k - \omega$ model provides the best estimates of the turbulent behavior of flow near the pipe wall and the free stream of the jet region of the model.

Due to the significant reduction in computational cost the RANS model is employed for the development of the CFD mesh establishing the flow field defining the initial conditions for the transient model. A transient model is required for evaluating flow noise, because of the temporal unsteadiness of turbulence and its relationship with eddy motions across a wide scale range. Thus, the CFD solution utilized as the input to Lighthill's Equation must be a transient solution that accurately predicts the motion of the turbulent eddies. In this study, a Large Eddy Simulation (LES) model using the WALE SGS model, as discussed in Section 2.3.4, is utilized to develop the time-dependent solutions.

5.3   Measurement

The measurements were completed according to the procedures discussed in Chapter 3 and the results are filtered for the BPF and electrical noise produced by the

flow rig. The filtered sound power results are given in Figure 5-2. As expected, the air

jet's noise is fairly broadband and matches the measurement results of Chapter 3.
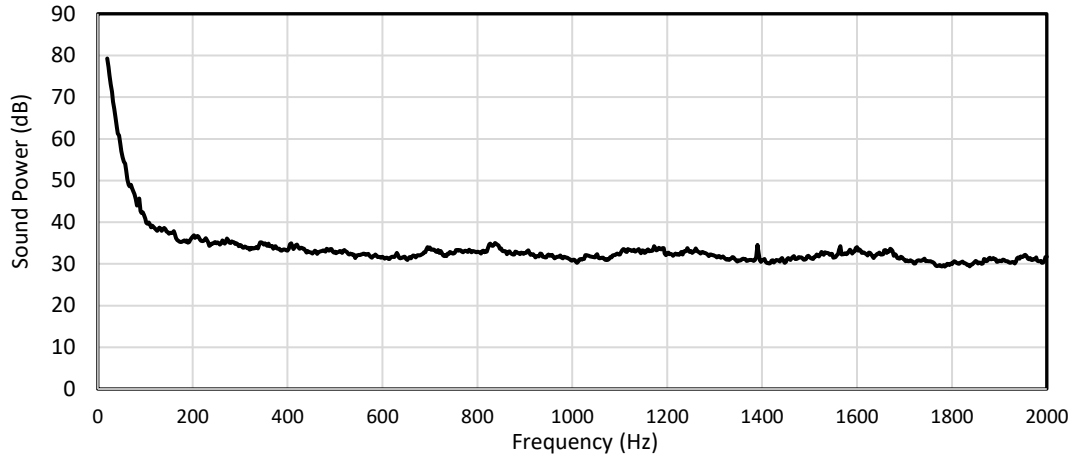
Figure 5-2 The measured sound power of the flow noise at the outlet of the 1.625 inch
OD pipe.

5.4   Construction and Results of the CFD Simulation

The CFD simulation was constructed using a full 3D model of a cylindrical pipe,

48 inches ($1.2\ m$) long, with an outer diameter of 1.625 inches ($41.3\ mm$) and a wall

thickness of 0.13 inches ($3.3\ mm$). The characteristic length of the model is the 1.495-

inch ($38.0\ mm$) inner diameter, denoted as d. At the pipe's end, a cylinder with a length

and diameter of $20d$ is employed to capture the turbulent jet region. The choice of the

$20d$ dimension for the modeled jet region is based on the recommendations in Pope [21]

and the scFLOW documentation [13]. To account for any potential effects at the pipe's

outlet, a $2d$ length of the outer pipe wall is included, as illustrated in Figure 5-2. The

fluid is defined as incompressible air, with the initial conditions of the RANS model set

at rest and at 20°C (room temperature).

The incompressibility assumption is considered largely valid for air at velocities less than Mach 0.3 [21][31]. Figure 5-3 depicts the applied boundary conditions of the CFD models. The pipe used for measurements has a smooth bore, and at the subsonic flow velocities the no-slip condition is deemed applicable, thus setting the flow velocity to zero at the wall. The boundaries of the modeled jet region have a static outflow pressure of zero applied, allowing the modeled air to move freely past these boundaries, equivalent to the air flowing freely into the unmodeled hemi-anechoic chamber. To further reduce computational costs, heat transfer was not considered, and only the momentum and continuity equations of the Navier-Stokes equations were solved.
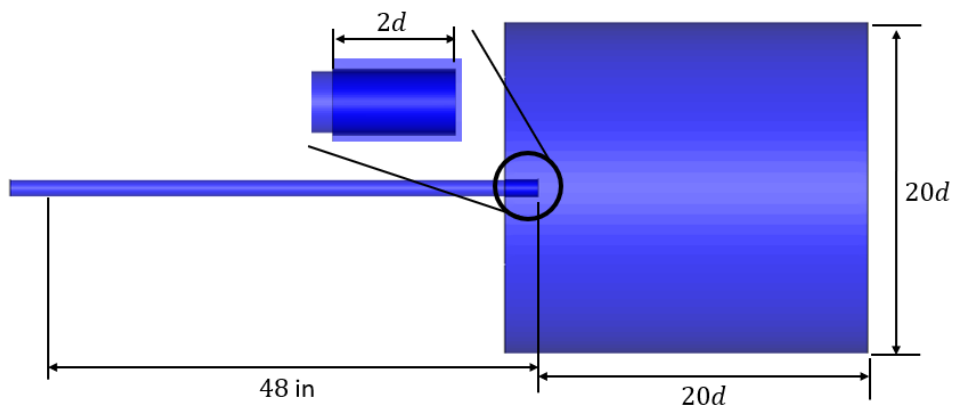
Figure 5-3 The 3D model used to construct the CFD simulation.

No-Slip Wall
Flow Velocity = 0

Normal Velocity
$25 \ m/s$

Static Outflow Pressure
Pressure = 0
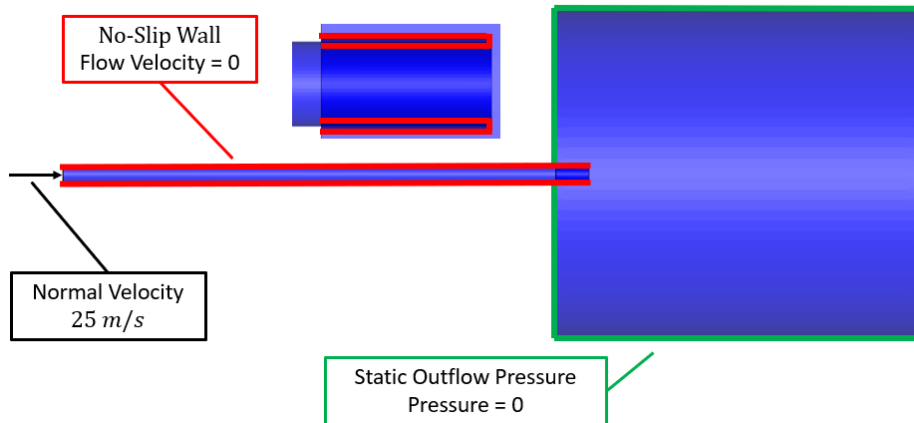
Figure 5-4 The boundary condition applied to the CFD domain.

5.4.1 Mesh Development

The CFD software scFLOW uses arbitrary polyhedron elements to construct the three-dimensional mesh. The Navier-Stokes equations are solved directly at the centroid of each element. The solution can then be interpolated between the element centroids. By only storing and saving information at the centroid of each element, the required memory is significantly reduced. The CFD mesh was developed iteratively using the RANS model and three parameters to define the mesh quality.

The first parameter used is the normalized wall coefficient (y^+), defined as

$$y^+ = \frac{y}{\nu}\sqrt{\frac{\tau_\omega}{\rho}} \leq 1 \qquad\qquad 5.6.1$$

where τ_ω is the wall shear stress, y is the distance of an element's centroid to a wall, and ν is the kinematic viscosity of the fluid. The normalized wall distance defines how well a mesh captures the boundary layer at a wall. A normalized wall distance of less than or equal to 1 is ideal and is critical in ensuring the accuracy of transient models. When

developing a mesh, the y^+ value is governed by the number of element layers that grow

thinner as the mesh approaches the boundary. The elements constructing the thin layers at

the boundary are typically referred to as the boundary layers. By iterating on the number

of layers of boundary layer elements at the pipe wall, 50 layers was found to be sufficient

for the final mesh. Figure 5-5 shows a zoomed in view of a section of the pipe wall and

the 50 layers of boundary layer elements. By the final iteration of the RANS model, all

101,400 boundary layer elements had a y^+ value of less than or equal to one.
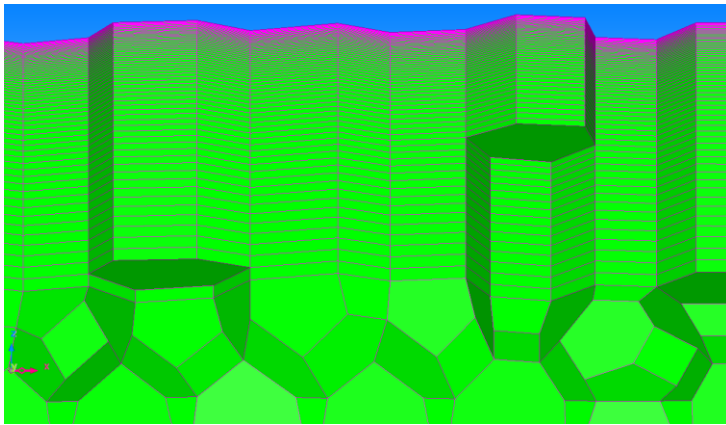
Figure 5-5 A zoomed in view of the 50 layers of boundary layer elements at the pipes
wall of the iteratively developed mesh

The second metric is unique to a CFD mesh planned for use in predicting

aeroacoustic phenomena. In turbulent flow, energy transfers from larger eddies down to

smaller eddies. The size of an eddy is inversely proportional to the frequency it

contributes to. Since a given CFD mesh can only resolve eddies of a certain minimum

size; the mesh size governs the maximum frequency a mesh can be used for. In this work

the target frequency was chosen to be $2000\ Hz$. The cut-off frequency of a given CFD

mesh is defined as

$$F_{cutoff} \approx \varepsilon^{1/3} \times \Delta x^{-2/3} \qquad 5.6.2$$

where Δx is the local element size of the mesh. Since F_{cutoff} is applicable to only areas of turbulent motion, the maximum frequency of a CFD mesh is defined by the F_{cutoff} for the regions where turbulent energy is maximized. The iCFD utility within Actran has built in capability to calculate the F_{cutoff} for a given CFD mesh. By postprocessing the turbulent energy data collected using the RANS model, the maximum frequency of the CFD mesh can be determined on a post hoc basis. From Figure 5-6, the maximum frequency of the CFD mesh was determined to be between 1800 and 2000 Hz .
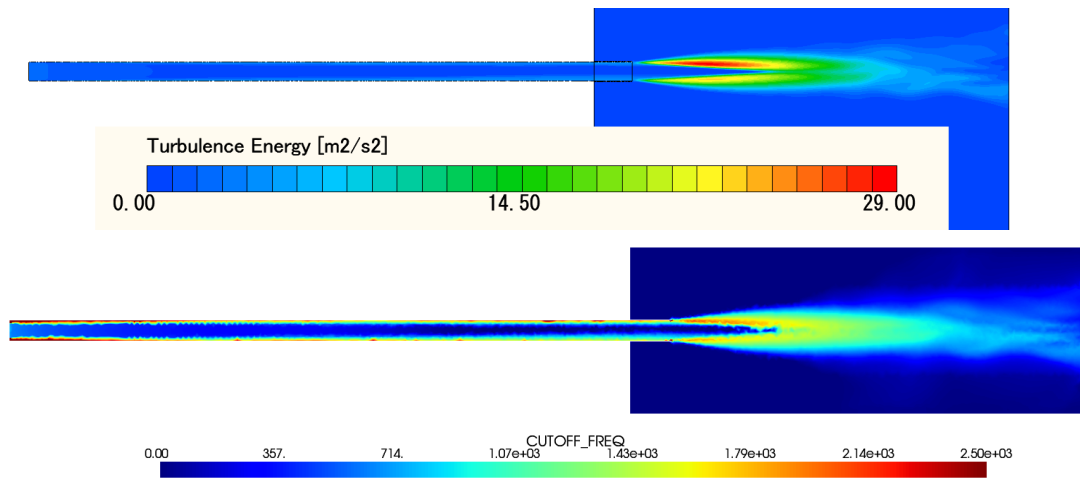
Figure 5-6 Comparison of the $F_{cut-off}$ of the CFD mesh as calculated using the Actran iCFD utility and the turbulent kinetic energy calculated from the CFD RANS model. Note that areas of high turbulent energy correspond areas with an F_{cutoff} of 1800 to 2000 Hz.

The final mesh quality metric used to develop the CFD mesh is the Courant-Friedrichs-Lewy (CFL) condition [32]. The CFL condition states

$$C = \frac{U\Delta t}{\Delta x} \leq C_{max} \qquad 5.6.3$$

where U is the flow velocity, Δt is the model's time step, and C is the nondimensional quantity referred to as the Courant number. C indicates over how many elements information travels in the unit of time between each solution cycle. According to the CFL condition, ideally the C of all the elements in a mesh is less than or equal to a maximum Courant number, C_{max}. The value of C_{max} depends on used time integration scheme of the model, but generally and in this work a value of 1 indicating that information travels from one element to the next without skipping elements is used. If the C of a given element is greater than one, then information will jump from one element to another while skipping others. In most application when information skips elements, accuracy is reduced and there is an increased risk of the solution having nonphysical results or diverging. Figure 5-7 illustrates how satisfying the CFL condition describes the travel of information through a mesh.
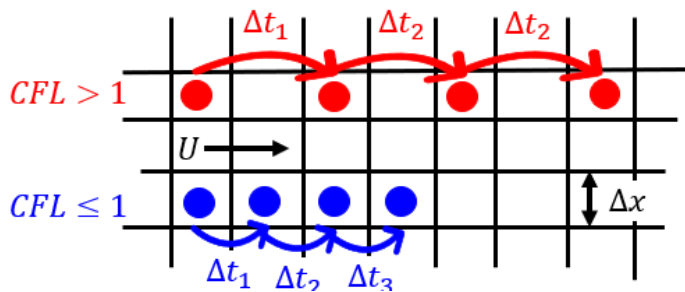
Figure 5-7 Illustration of how information travels within a CFD mesh based on the value of the Courant number. Red indicates the case in which the CFL condition is not satisfied, and the Courant number is greater than 1. Blue then indicates how information travels through a mesh when the Equation 5.6.3 is satisfied.

In practice, refining a mesh such that all elements satisfy Equation 5.6.3 is typically impractical and can cause an overly fine mesh increasing computational time of the model. Thus, the CFL condition is typically best satisfied using local refinement of

the mesh. To simplify and accelerate the process of developing the CFD, the target CFL condition was chosen to be

$$\overline{C} \leq 0. \qquad\qquad\qquad 5.6.4$$

where $\overline{C}$ is the average Courant number for the entire mesh. To ensure Equation 5.6.4 is satisfied, the RANS model is used to calculate an average pseudo time step for the mesh. The average pseudo time step is then used to determine the maximum time step possible that will satisfy Equation 5.6.4 for a transient analysis. The mesh was then modified in localized areas to ensure the desired transient time step was able to satisfy Equation 5.6.4. The solved for average pseudo time step for the final mesh is $6.9E$-5 seconds, thus a time step of $5E$-5 was chosen for the transient LES model. Figure 5-8 shows $\overline{C}$ for the total run time of the LES model which satisfied the chosen CFL condition given by Equation 5.6.4. To confirm the selected CFL condition resulted in a usable mesh, the Courant number of the individual elements was reexamined after solving up to 0.125 seconds in LES model. Figure 5-9 shows a cross-section of the model with the individual element's Courant numbers plotted.

The decision to proceeded with the CFL conditions not completely satisfied was decided based on the level of convergence seen in the extrema pressure and velocities at the completion of the LES model up to time 0.125 seconds as shown in Figure 5-10. Based on the recommendations provided in the scFlow manual [13] the very small variations in the extrema pressure and velocities seen from 0.06 to 0.12 seconds demonstrated that the model had not diverged, thus not completely satisfying the standard CFL condition was deemed acceptable.
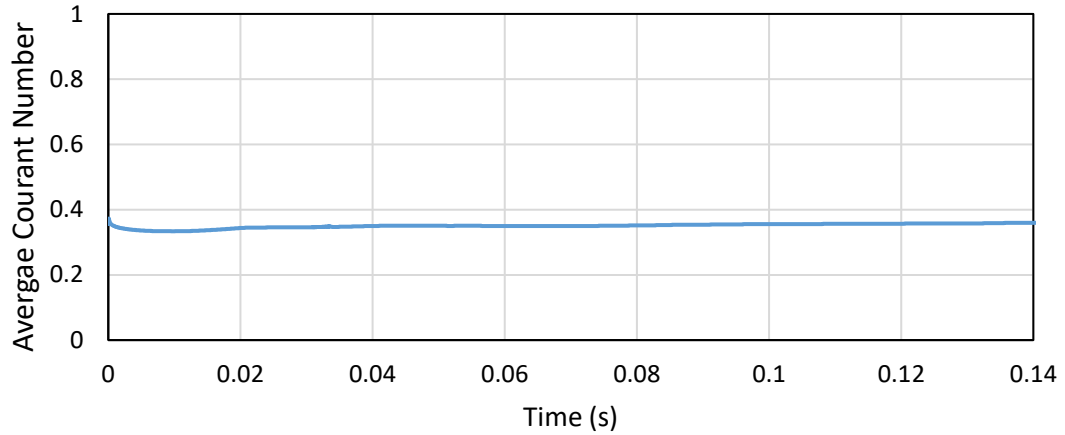
Figure 5-8 The average Courant number for the total runtime of the LES transient model using a time step of $5E$-5 seconds. The average Courant number of the mesh during the LES run satisfied the target requirement given by Equation 5.6.4.
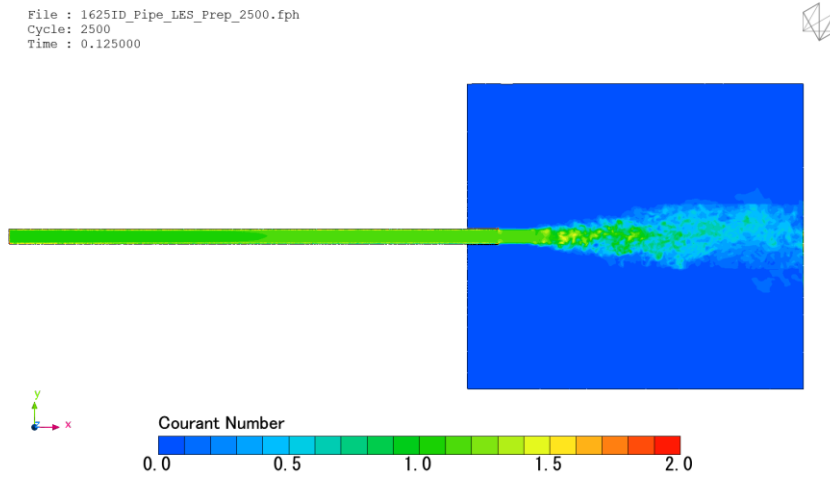
Figure 5-9 Cross-section of the XY-Plane of the mesh's Courant number at time step 0.125 seconds. Most elements of the elements outside of the boundary layer have Courant numbers between 1 and 1.5

The decision to proceeded with the CFL conditions not completely satisfied was decided based on the limited range seen in the extrema pressure and velocities at the completion of the LES model up to time 0.125 seconds as shown in Figure 5-10. Based on the recommendations provided in the scFlow manual [13] the limited range of the

extrema pressure and velocities seen from 0.06 to 0.12 seconds demonstrated that the

model had not diverged, thus not completely satisfying the standard CFL condition was

deemed acceptable.
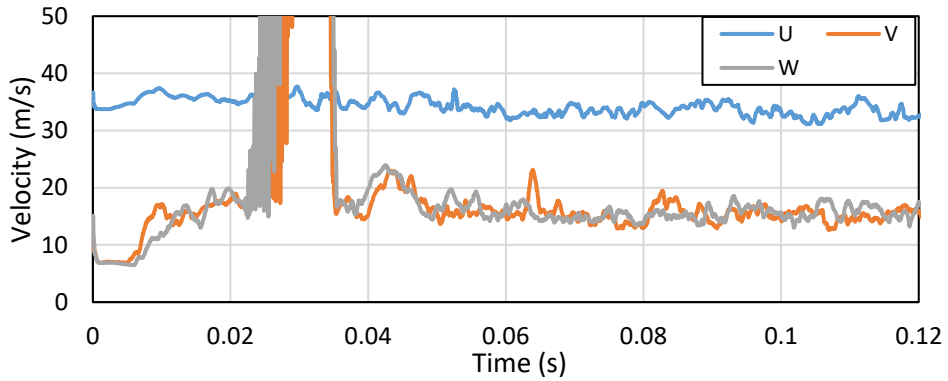
(a)
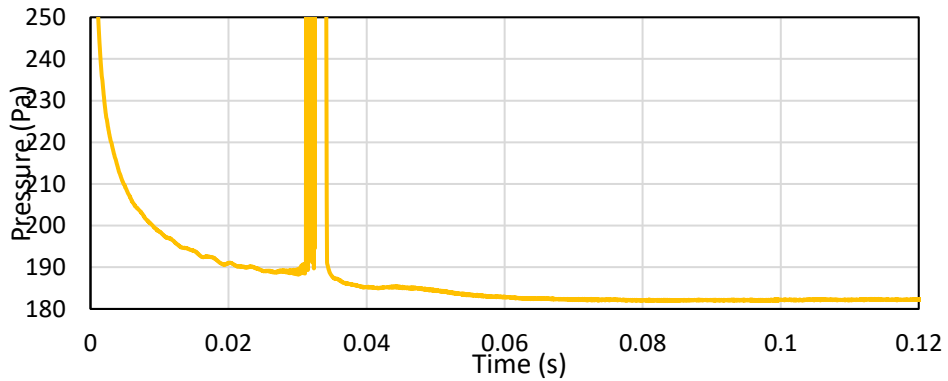
(b)

Figure 5-10 The extrema of the (a) velocities and (b) pressure for the 0.125 seconds of
the LES transient model.The velocities of the x,y and z directions in terms of the U,V
and W vectors respectively. By 0.06 seconds the extrema of the velocity and pressure
had stabilized to only fluctuate within a constant range.

Using the three metrics and an iterative process, the mesh developed for the

steady-state and transient solutions consisted of 28.2 million nodes and 19.8 million

elements. Figure 5-11 shows the mesh used for the RANS and LES models completed in

this work.
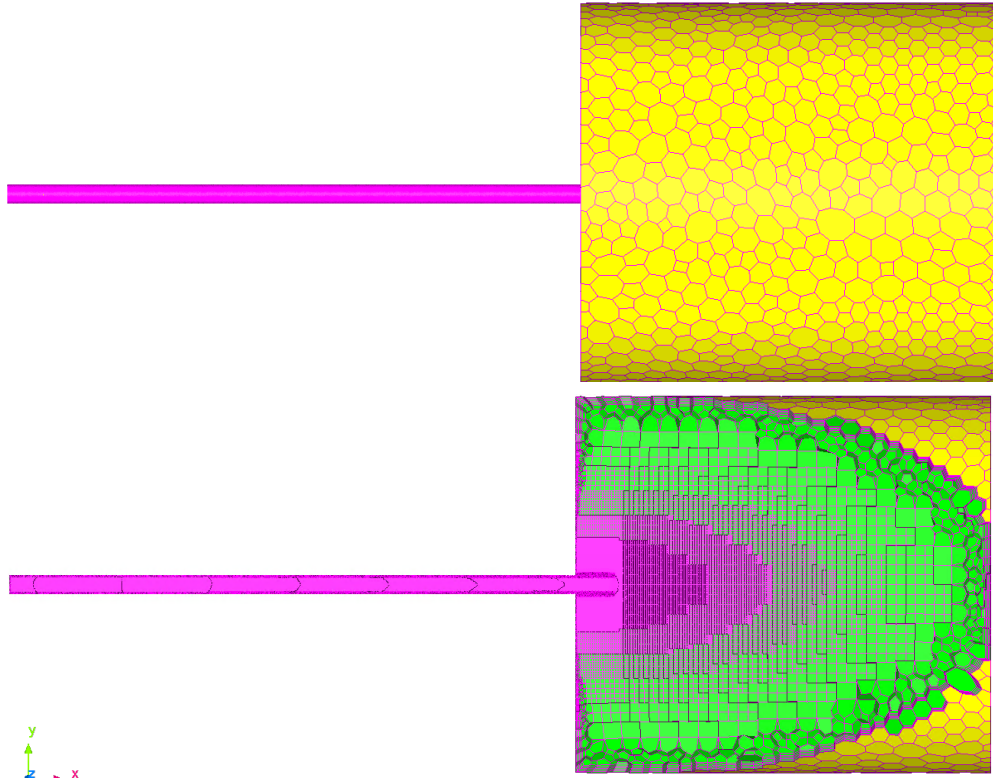
Figure 5-11 The final CFD mesh as iteratively developed using the RANS model and the three parameters that defined mesh quality.

5.4.2 RANS Model Statistics and Results

Figure 5-12 shows the final x-direction velocity results of the RANS model. This solution was developed after 500 solution cycles. The residual values for the 500th cycle of the RANS model is provided in Table 5-1. The turbulent energy dissipation rate achieved a tight convergence in the range of 1E-8 while all other metrics reached a loose convergence of approximately 1E-4.

To correlate the RANS model to the collected measurement data, the centerline velocity at the pipe outlet was compared. The RANS model predicted a centerline velocity of 33 to 34 m/s, while the measured outlet velocity was at 32 m/s. This variance of 1 to 2 m/s between the measurement and the model was considered to be

acceptable. It is reasonable to assume that this variance is due to inaccuracies in the

measurement and the assumption of the pipe wall being frictionless with no heat transfer.

Table 5-1 Final residual values for the RANS model. Note all values
indicate a loose to tight convergence of the final solution.

Monitored Convergence Parameters	RMS Residual
X-Direction Velocity, U_x	5.18E-04
Y-Direction Velocity, U_y	4.44E-04
Z-Direction Velocity, U_z	4.09E-04
Pressure, p	1.90E-04
Turbulent Kinetic Energy, k	1.94E-04
Turbulent Energy Dissipation Rate, ω	5.72E-08

Velocity (x-component) [m/s]

−12.00   11.00   34.00
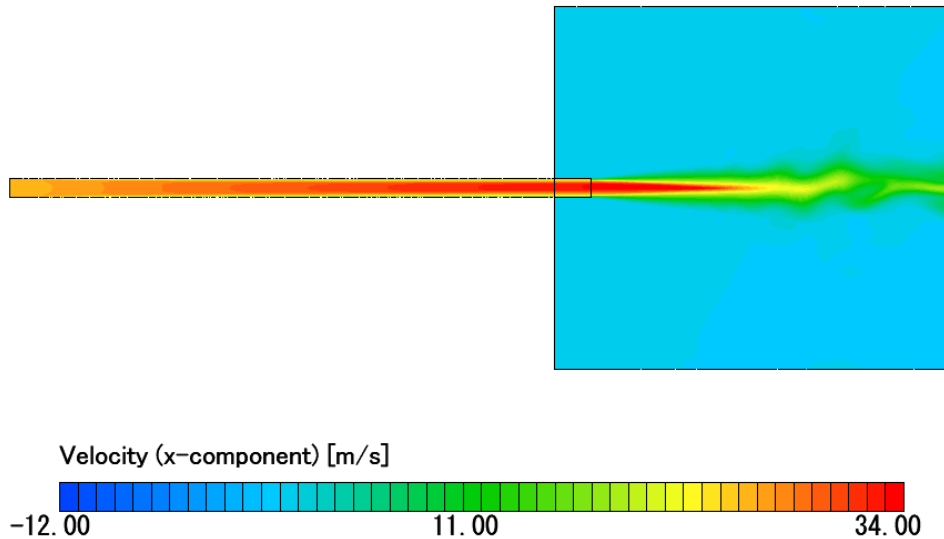
Figure 5-12 Cross-section of the magnitude of the x-direction velocity vector as
solved using the completed RANS model. The center line velocity at the pipes outlet
was used here to validate the RANS model solution to the measurement.

5.4.3   LES Model Statistics and Results

The ultimate outcome of the RANS model serves as the basis for establishing the

initial conditions and developing the mesh for use in the LES model. From Lighthill's

equation (Equation 5.2.4), the velocity vectors are the essential inputs for defining the

acoustic sources. The LES model is used to solve for the velocity vectors with respect to time.

The transient LES model consisted of two runs. The initial run, designated as LES Prep, encompassed 2500 cycles with a time step of 5E-5 seconds, resulting in a total CFD run time of 0.125 seconds. The primary objective of this run was to remove the effect of the assumptions derived from the inputted RANS model solution and to check the mesh quality using the afore mentioned mesh quality metrics. Data collection during the LES Prep run was restricted to the first and final cycles to minimize memory requirements. In Figure 5-13, contour maps show the magnitude of the x-direction velocity vector at 0.005 s and 0.125 s. From Figure 5-10 the maximum velocities and pressure in the model versus the time step can be seen. It is noteworthy that the spike in the extrema seen at time 0.05 seconds, underscores the importance of running the LES model for an extended duration before gathering data for formulating acoustic sources, particularly when utilizing a steady-state model to establish the initial conditions.
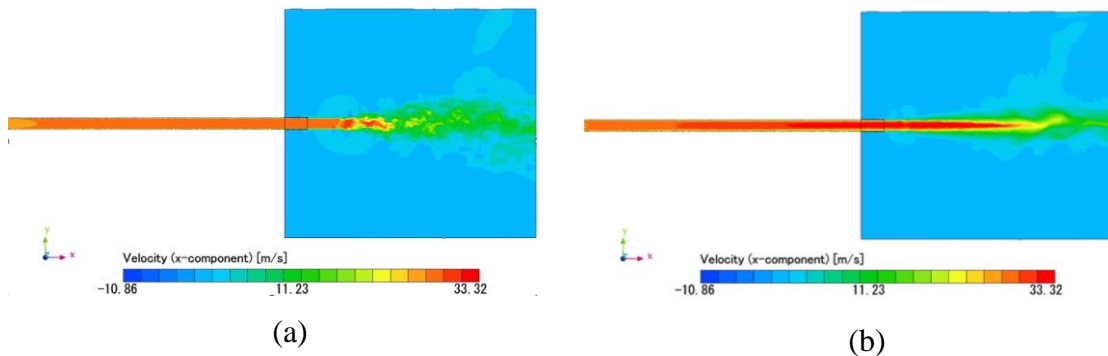
Figure 5-13 Cross-section of the LES Prep run (a) after the first-time step of 0.005 seconds and (b) at the runs end after 0.125 seconds.

The second phase of the LES model, referred to as LES Sampling, had its initial conditions determined by the final time step of the LES Prep model. The primary

objective of the LES Sampling run was to accumulate time samples for the formulation of

acoustic sources and subsequent conversion into the frequency domain using FFT. There

were 6000 total time steps with an increment 5E-5 seconds, resulting in a total runtime of

0.3 seconds. Data on the velocity vector was gathered every 2 cycles, leading to a time

step of the collected data being 1E-4 seconds. Figure 5-14 presents a selection of color

contour maps illustrating the velocity vector at various time steps collected during the

LES Sampling run.
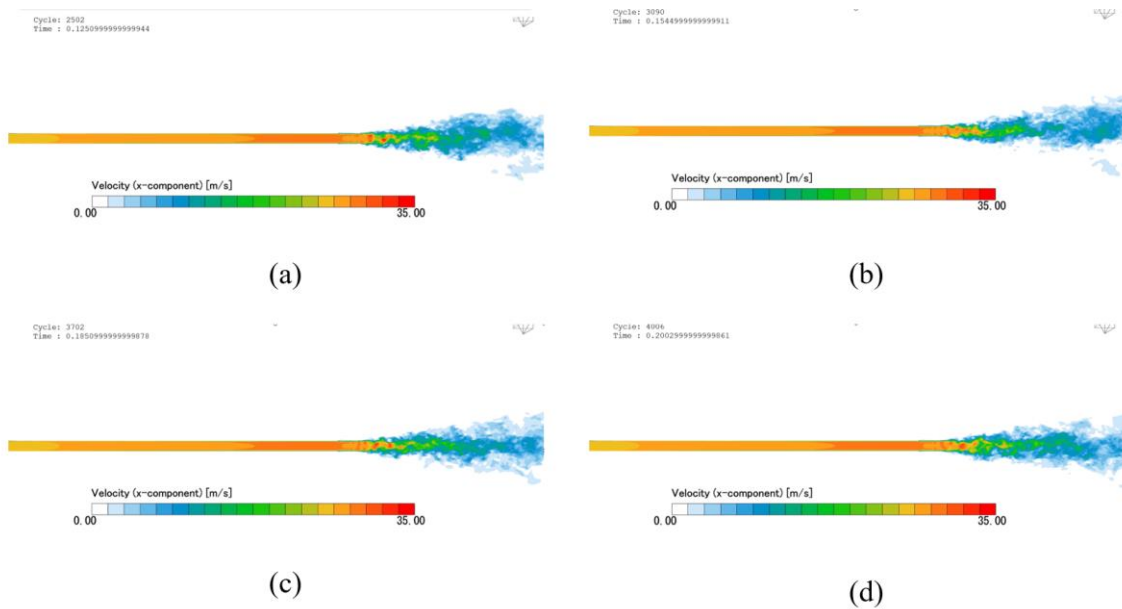
Figure 5-14 A selection of the x-direction velocity results of the LES Sampling run. (a) to (d) step forward in time with (a) cycle 2 at $0.1251\ s$, (b) cycle 590 at $0.1545\ s$, (c) cycle 1202 at $0.1851\ s$ and (d) cycle 1506 at $0.2003\ s$.

5.5   Acoustic Model

The acoustic model was meshed and constructed in Actran. The recommended

element size is 8 elements per acoustic wavelength [33][34]. To reduce the computational

cost and the total run time an adaptive mesh was used in the acoustic model. A total of

eight meshes were constructed for eight frequency ranges as given in Table 5-2.

Table 5-2 The frequency ranges for the eight meshes created by
the adaptive mesh

| Mesh	Mesh Frequency Range (Hz)
1	20 - 100
2	110 - 500
3	510 - 800
4	810 - 900
5	910 -1000
6	1010 - 1500
7	1510 - 1650
8	1660 - 2000

The applied boundary conditions of the acoustic model are shown in Figure 5-15.

The bay doors of the anechoic chamber sealed around the pipe were modeled as having a

unit absorption coefficient. The rest of the chamber was modeled as non-reflecting using

infinite elements on the boundary of the model. The floor of the chamber was modeled as

a reflective surface with a normal particle velocity of zero. The inlet of the pipe was

given the measured source impedance of the flow rig without flow from Chen[5]. For

validating the model to the completed measurement eight microphone points were

defined to match the measurement locations. As shown in Figure 5-16, the aeroacoustic

source region comprises both the pipe and jet areas. The jet region is delineated by a

cylindrical space with the same length as the CFD model but half the diameter.
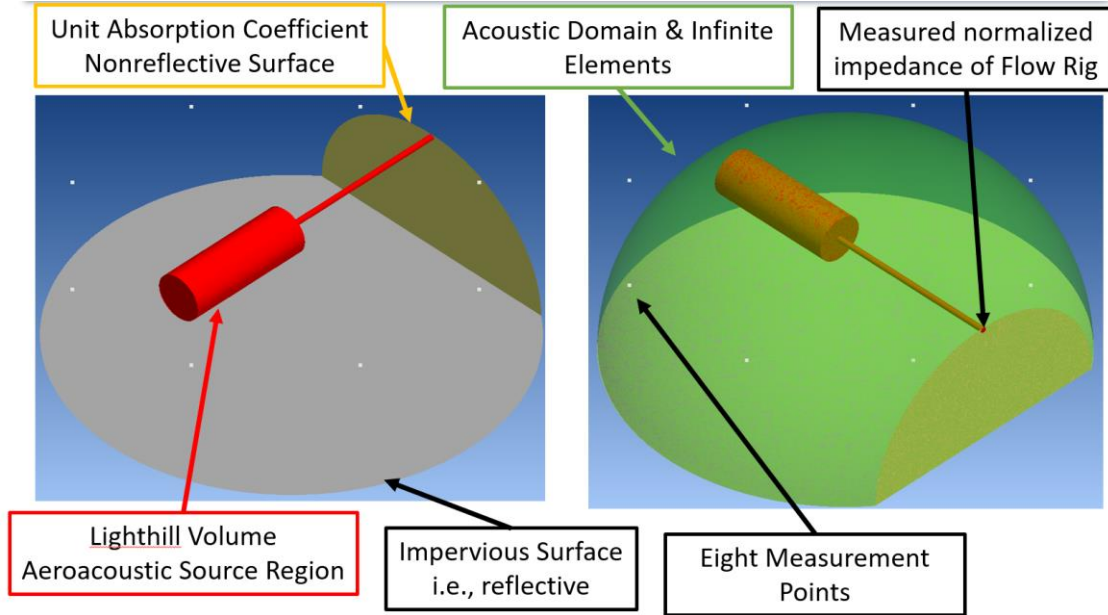
Figure 5-15 The applied boundary conditions of the acoustic model

5.5.1   Signal processing and Conversion to Frequency Domain

The conversion of time-domain sources to the frequency domain involves utilizing a Direct Fourier Transform. Similar to working with measured time-data, special attention is required for the conversion from time-domain CFD results. The total run time and time step of the collected CFD data samples establish the minimum frequency, frequency step size, and the maximum frequency of the final acoustic solution. To adhere to the Nyquist-Shannon theorem and prevent spectral aliasing, the determined maximum frequency of the acoustic model must satisfy the condition:

$$\frac{1}{\Delta t} \geq 4 f_{max} \qquad\qquad 5.5.1$$

Note that due to the Lighthill volume source, a slight modification is necessary because of the product of velocities defining T_{ij}. The minimum frequency and frequency step size are given by:

89

$$f_{min} = \Delta f = \frac{1}{T_{CFD}} \qquad\qquad 5.5.2$$

where T_{CFD} is the total runtime of the collected CFD time steps.

To address turbulence randomness and smooth the resulting spectrum data, five time series with 50% overlap are sampled from the collected CFD time data. Each time series, as depicted in Figure 5-16, is 0.1 seconds long. The length of a single time series defines T_{CFD}. From Equation 5.5.2, it is determined that the minimum frequency and frequency step size for the simulation are 10 Hz. Using the 1E-4 time step of the collected CFD data, the maximum frequency of the collected data is found to be 2500 Hz. It is important to note that the limiting factor to the maximum solvable frequency is F_{cutoff}, estimated to be approximately between 1800 and 2000 Hz. Finally, a Hanning window is applied to address signal discontinuities, and a power spectral density correction is implemented to account for the different durations of the measured and simulated time signals.
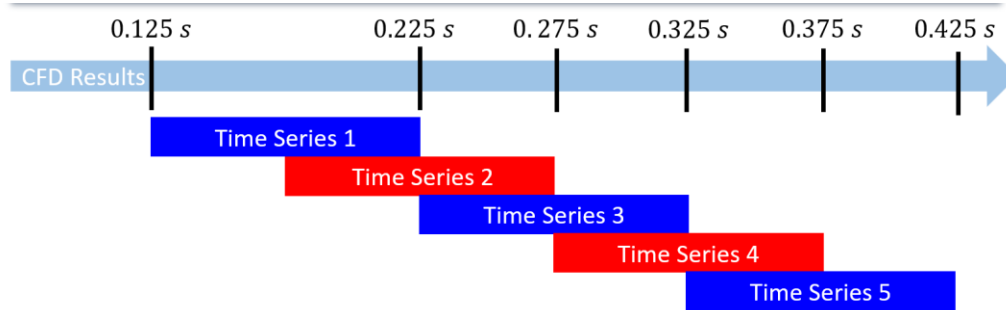
Figure 5-16 The breakdown of the 5-time series that the simulated data was broken down into.

5.5.2 Truncation Filter

Unsteady turbulent sources at the periphery of the CFD domain are subject to truncation. These structures are anticipated to exhibit decreased accuracy owing to the impact of boundary conditions and mesh coarsening near the outlet boundaries of the CFD model. The truncated structures give rise to pronounced artificial dipole sources in the acoustic solution. Consequently, these structures are eliminated from the final acoustic solution through the application of a truncation filter.

The most basic form and the Actran generic variant of a truncation filter operates by multiplying the source values at each node by a cosine function. At the center of a Lighthill volume source, the cosine function is set to unity, and as you progress toward the boundaries, the filter gradually diminishes, approaching zero, as illustrated in Figure 5-17. The rate at which the cosine function approaches 0 is determined by a thickness value. In this study, an exploration of varying thickness values—0.05, 0.1, and 0.25 meters—is conducted as part of the results analysis.

$$w(\vec{x}) = 1 \;\rightarrow \text{source conserved}$$
$$w(\vec{x}) = 0 \;\rightarrow \text{source removed}$$
$$1 > w(\vec{x}) > 0 \rightarrow \;\text{smooth damping (cosine function)}$$
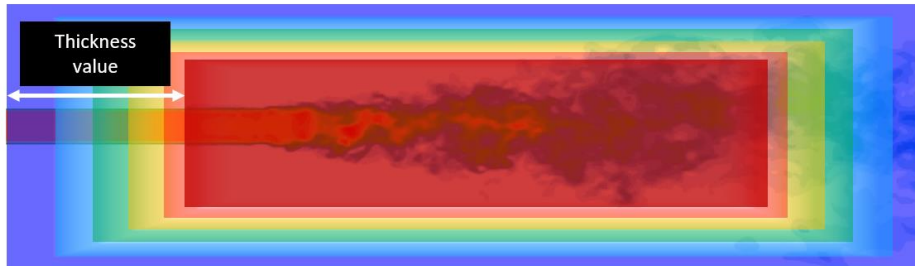
Figure 5-17 Illustration of the simple cosine truncation filter used in this work and built in to the Actran software. .

5.6   Summary of the Simulations Results

In Figure 5-18, the outcomes using a 0.05 meter thickness value for the truncation filter are presented. The simulation results exhibit a weak correlation below 200 Hz. Subsequently, a robust correlation between the measurement and the simulation is observed up to approximately 1400 Hz. However, around 1400 Hz, there are discrepancies between the simulation and measurement.
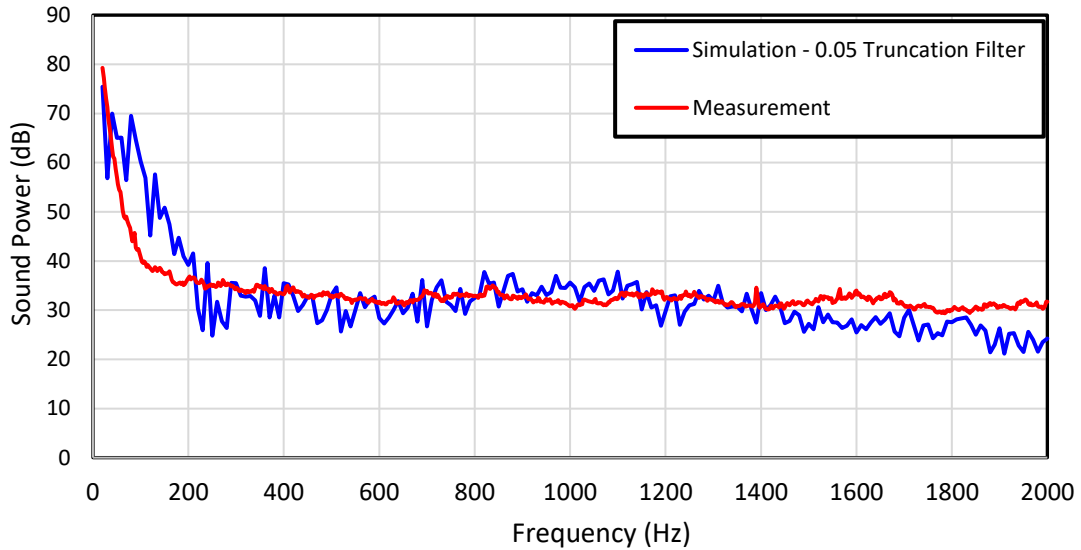
Figure 5-18 Comparison of the CAA model's results using 0.05 meter thickness a value for the truncation filter.

When employing a 0.1 meter thickness value for the truncation filter, some enhancement in the frequencies below 200 Hz becomes apparent, as illustrated in Figure 5-19. However, above 1400 Hz, there is no discernible difference in the simulation results between the 0.05 and 0.1 meter thickness values. This suggests that the inaccuracy of the model below 200 Hz is a consequence of the truncation filter, while the underprediction of the model above 1400 Hz is likely attributed to the F_{cutoff} of the CFD mesh.

Issues with the truncation filter can be easily identified by examining a contour map of the sound pressure level. Figure 5-20 presents such a comparison at 80 Hz, where the most significant change in amplitude of the simulation results is observed. It is noteworthy that the pronounced source at the front edge of the Lighthill volume source region, with the 0.05-meter truncation filter applied, is considerably reduced with the 0.1-meter truncation filter, aligning more closely with the expected noise level from a subsonic jet.
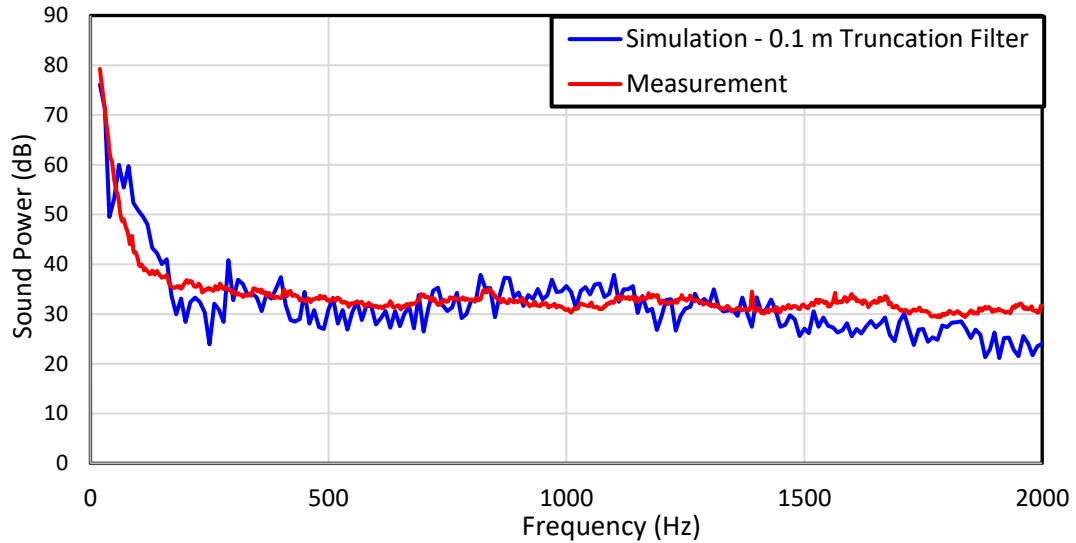
Figure 5-19 Comparison of the CAA model's results using 0.1 meter thickness a value for the truncation filter.

Truncation Filter – 0.05 m Truncation Filter – 0.1 m
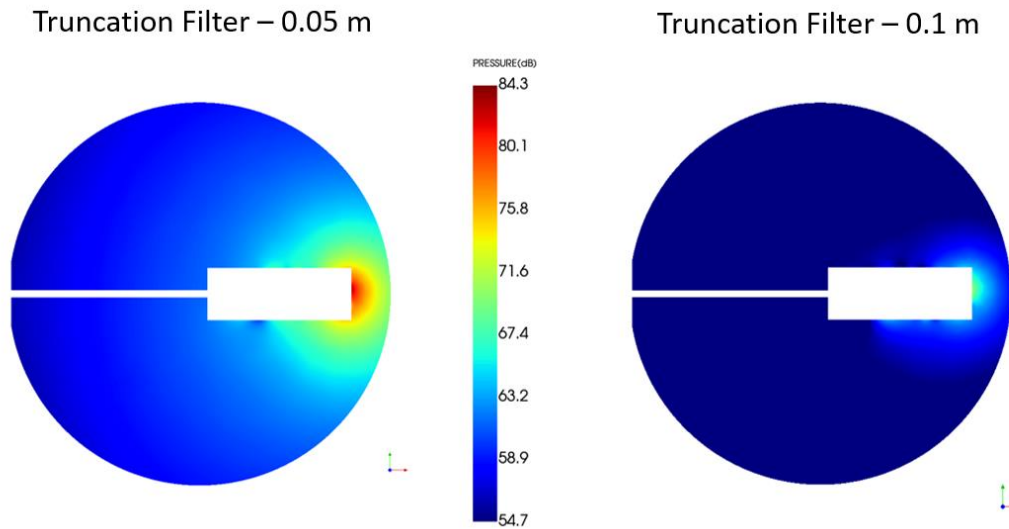
Figure 5-20 Comparison of sound pressure levels at 80 Hz with a 0.05 and 0.1 meter truncation filter.

As increasing the truncation filter clearly improved the results further increasing the thickness value to 0.25 meters was investigated. Figure 5-21 shows the simulation results with a 0.25 meter thickness value truncation filter applied. The model now over

predicts the sound power from about 80 Hz to 1000 Hz. Above 1000 Hz the model under

predicts the sound power of the subsonic jet.
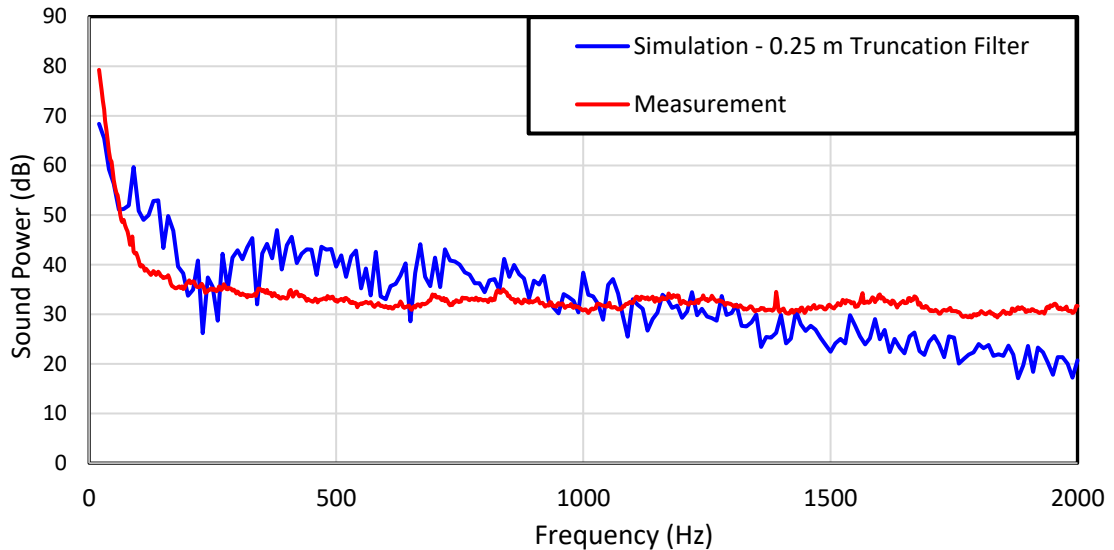
Figure 5-21 Comparison of the CAA model's results using 0.25 meter thickness a value for the truncation filter

5.7   Summary

In this study, the combination of the commercially available CFD software

scFLOW and the acoustic finite element software Actran has proven successful in

simulating the flow noise of a subsonic jet using hybrid computational aeroacoustics

(CAA) methods. The CAA simulation results exhibited a robust correlation with

measured data up to 1400 Hz when employing a simple 0.1 meter truncation filter, as

depicted in Figure 5-20. Notably, all simulation tasks were accomplished using a standard

eight-core workstation with 128 GB of memory, demonstrating the hybrid CAA approach

as a methodology with a computational cost conducive to practical use within the

industry.

The model's accuracy was found to hinge on careful tuning of the truncation filter and the utilization of a high-quality, well-tuned CFD model. The CFD model necessitates a finely tuned mesh to ensure the desired frequency step size, minimum frequency, and maximum frequency of the acoustic model are attained. The final CFD model used here could be further optimized for computational cost and accuracy by further refining the mesh.

Finally, the truncation filter must be carefully tuned to prevent the generation of artificial dipoles from truncated turbulent eddies while avoiding the removal of an excessive number of critical eddies essential for determining the acoustic field. Future endeavors should encompass further enhancements to the CFD mesh to achieve the targeted 2000 Hz maximum frequency, satisfaction of the CFL condition, and the development of a more advanced truncation filter to accurately eliminate the effects of truncated eddies from the acoustic solution.

CHAPTER 6. SUMMARY AND FUTURE WORK

The primary objective of this work was to develop and demonstrate techniques for the analysis and characterization of aeroacoustic phenomena. Though the study of aeroacoustics has advanced significantly from the works of Lighhill, Curle, Daves and Ffwocs Williams, their fundamental theories are critical to characterizing subsonic aeroacoustics. Thus, in Chapter 3 using their theories the muffler test rig at the University of Kentucky was demonstrated to be able to generate and measure aeroacoustic sources for flow velocities up to Mach 0.3.

Chapter 4 then used the test rig to analyze flow noise generated by concentric tube resonators a common muffler component. The flow noise generated by concentric tube resonators is studied experimentally as the phenomena is time dependent and cannot be defined using Lighthill's analogy. In this study it was found that the frequency of the whistle generated by a concentric tube resonator is controlled by the hole diameter of the perforate and that minimizing the percentage of open area of the perforate was critical in controlling the amplitude of the whistle.

Though this measurement campaign generated a large useful data set and a selection of conclusion on the nature of the whistle noise of concentric tube resonator, test rigs like University of Kentucky's flow rig are not always practical to develop and maintain. Thus, Chapter 5 demonstrated the capabilities of current commercial finite element codes in simulating and predicting aeroacoustic noise. Using the Hybrid approach, a CFD and acoustic FEM were used to accurately predict the noise from the jet at the outlet of straight pipe. This simulation was validated using the measurement data from Chapter 3.

97

From the construction of the models, it was found that the truncation filter which helps to define the edges between the acoustic and fluid domains, is one of the most critical parameters in developing an accurate hybrid aeroacoustic model.

6.1   Future Work

The rig should be used to continue research into flow noise generated by muffler elements and perforates. Treatments for the whistle noise generated by concentric tube resonator is the logical next step from this work. Additionally, work could be done on the effects of flow forced through perforates or a grazing flow across a perforate. Finally, the rig could be used to measure a wide variety of flow noise phenomena in mufflers such as the effects of the outlet geometry on jet noise, noise from jet impediment either in expansion chambers or through orifices, and the noise from mixing or cross flows. From the work in computational aeroacoustics, by increasing the computational resources available more complex geometries could be simulated. An expansion chamber and then a concentric tube resonator being the logical first choice due to the available data set created here. Combined with the experimental work completed using the muffler test rig the option for experimentally validated CAA simulations example grows endlessly. By combing the experimental and computational methodologies described in this work, future researchers can complete in-depth analysis of a wide variety of aeroacoustic phenomena. Some such examples include perforate hole geometry impact on both acoustic and flow performance, muffler expansion chamber geometry's effect on jet impingement, and outlet geometry impact on jet noise.

The options listed here are in no way all encompassing, as the combination of the experimental and computational method given here, creates a near endless list of research options. It is anticipated that both the experimental work using the muffler test rig and the computational work will be expanded on by future students. It's the hope of this author that the muffler test rig and the computational methods given in this work lay fertile ground, from which a range of research and studies can be based upon.

REFERENCES

1. Joseph W. Sullivan; A method for modeling perforated tube muffler components. II. Applications. J. Acoust. Soc. Am. 1 September 1979; 66 (3): 779–788. https://doi.org/10.1121/1.383680 T. Elnady, "A Platform to Measure Transmission Loss of Mufflers with Flow," INTER-NOISE Conference Proceedings, (2007).

2. H. Kim, "Transmission loss of silencers with flow from a flow-impedance tube using burst signals," The Ohio State University, ProQuest Dissertations Publishing, (2011).

3. H. Howell, Personal Correspondence, (2020-2023).

4. Chen, J., "Development of a Muffler Insertion Loss Flow Rig," Master's Thesis, University of Kentucky, 2019.

5. D. A. Bies, C. H. Hansen, C. Q. Howard, "Engineering Noise Control," CRC Press, Taylor and Francis Group, (2018).

6. Lighthill, Michael James. "On sound generated aerodynamically I. General theory." Proceedings of the Royal Society of London. Series A. Mathematical and Physical Sciences 211.1107 (1952): 564-587.

7. Lighthill, Sir M. J., 2001. *Waves in Fluids*. Cambridge University Press

8. Blake, William K. 2017. *Mechanics of Flow-Induced Sound and Vibration V1*. Academic Press

9. Curle, N. 1955. *The Influence of Solid Boundaries Upon Aerodynamic Sound*.

10. Davies, H. G., and J. E. Ffowcs Williams. 1968. "Aerodynamic Sound Generation in a Pipe." *Journal of Fluid Mechanics*, no. 4 (June): 765–78. https://doi.org/10.1017/s0022112068001011

11. Fox, R W, et al. *Introduction to Fluid Mechanics*. Hoboken, N.J., Wiley & Sons, 2010.

12. Cradle scFLOW User's Guide (2021).

13. Jones, W.P, and B.E Launder. 1972. "The Prediction of Laminarization with a Two-Equation Model of Turbulence." *International Journal of Heat and Mass Transfer*, no. 2 (February): 301–14. https://doi.org/10.1016/0017-9310(72)90076-2.

14. Kolmogorov, A. (1962). A refinement of previous hypotheses concerning the local structure of turbulence in a viscous incompressible fluid at high Reynolds number. *Journal of Fluid Mechanics, 13*(1), 82-85. doi:10.1017/S0022112062000518

15. Wilcox, D.C. (1988), "Re-assessment of the scale-determining equation for advanced turbulence models", AIAA Journal, vol. 26, no. 11, pp. 1299-1310.

16. Wilcox, D. C., "Formulation of the k-omega Turbulence Model Revisited," AIAA Journal, Vol. 46, No. 11, 2008, pp. 2823-2838, https://doi.org/10.2514/1.36541.

17. Wilcox, D. C., Turbulence Modeling for CFD, 3rd edition, DCW Industries, Inc., La Canada CA, 2006.

18. Menter, F. R. 1992. "Influence of Freestream Values on K-Omega Turbulence Model Predictions." *AIAA Journal*, no. 6 (June): 1657–59. https://doi.org/10.2514/3.11115.

19. Menter, F., "Zonal two equation k-ω turbulence models for aerodynamic flows," *AIAA* 93-2906, (1993).

20. Pope, S. B., and Stephen B. Pope. 2000. *Turbulent Flows*. Cambridge University Press.

21. Temmerman, L., Leschziner, M. A., Mellen, C. P., and Fröhlich, J., "Investigation of wall-function approximations and subgrid-scale models in large eddy simulation of separated flow in a channel with streamwise periodic constrictions," *Int. J. Heat Fluid Flow*, Vol. 24, (2003), pp.157-180.

22. VDI 3733, "Geräusche bei Rohrleitungen [Noise at Pipes], Verein Deutscher Ingenieure [Association of German Engineers], 1996.

23. Kuhn, G.F. and Morfey, C.L., "Noise Due to Fully Developed Turbulent Flow Exhausting from Straight and Bent Pipes," Journal of Sound and Vibration 1, no. January (1976): 27-35. https://doi.org/10.1016/0022-460x(76)90704-5.

24. Ducret, F., "Studies of Sound Generation and Propagation in Flow Ducts," Licenciate Thesis, The Royal Institute of Technology, 2006.

25. Davies, P.O.A.L., Bento Coelho, J.L., and Bhattacharya, M., "Reflection Coefficients for an Unflanged Pipe with Flow," Journal of Sound and Vibration 4, no. October (1980): 543-546. https://doi.org/10.1016/0022-460x(80)90364-8.

26. Fukuda, Motokazu, Naoya Kojima, and Tohru Iwaishi. 1983. "A Study on Mufflers with Air Flow : 1 St Report Generation of Noise from Expansion Cavity Type Mufflers Due to Mean Flow." *Bulletin of JSME*, no. 214: 562–68. https://doi.org/10.1299/jsme1958.26.562.

27. Izumi, Haruo, Naoya Kojima, and Motokazu Fukuda. 1985. "A Study on Mufflers with Air Flow : 2nd Report Various Methods for the Reduction of Air Flow Noise." *Bulletin of JSME*, no. 238: 631–37. https://doi.org/10.1299/jsme1958.28.631

28. Kojima, Naoya, Yukiharu Nakamura, and Motokazu Fukuda. 1987. "A Study on the Correlation between Fluctuating Velocity in a Muffler and Air Flow Noise." *JSME International Journal*, no. 265: 1113–20. https://doi.org/10.1299/jsme1987.30.1113.

29. Yamada, Tatsuya, Takehiko Seo, Masato Mikami, and Takashi Esaki. 2013. "Characteristics of Whistle Noise from Mufflers with Perforated Pipes." *The Journal of the Acoustical Society of America*, no. 5 (May): 3363–3363. https://doi.org/10.1121/1.4805746.

30. Ueyama, Atsushi. n.d. "Want to Know More! Basics of Thermo-Fluid Analysis 16: Chapter 3 Flow 3.3.2 Compressibility and Incompressibility (1) List." Cradle CFD | Smart Multiphysics Focused CFD Simulation | Hexagon. Accessed November 13, 2023. https://www.cradle-cfd.com/media/column/a149.

31. Courant, Richard, et al. *On the Partial Difference Equations of Mathematical Physics*. *Internet Archive*, New York: Courant Institute of Mathematical Sciences, New York University, 1956, archive.org/details/onpartialdiffere00cour/mode/2up?view=theater. Accessed 21 Apr. 2024.

32. MSC Actran User's Guide (2022)

33. Åbom, Mats. 2008. An Introduction to Flow Acoustics

34. Chanaud, R. C., and Alan Powell. 1965. "Some Experiments Concerning the Hole and Ring Tone." The Journal of the Acoustical Society of America, no. 5 (May): 902–11. https://doi.org/10.1121/1.1909476.

35. Donkin, S. and Herrin, D.W., "Measurement of Sound Power Due to Flow Noise at the Outlet of a Straight Pipe," SAE Technical Paper 2021-01-1050, 2021, doi:10.4271/2021-01-1050.

36. Donkin, S., and Herrin, D.W. "An experimental study of flow-induced noise from perforated pipes." INTER-NOISE and NOISE-CON Congress and Conference Proceedings. Vol. 264. No. 1. Institute of Noise Control Engineering, 2022.

37. Donkin, S., and Herrin, D.W. "Validation of the Computational Aeroacoustic Simulation of a Subsonic Jet tailpipe Flow Noise." INTER-NOISE and NOISE-CON Congress and Conference Proceedings. Vol. 266. No. 2. Institute of Noise Control Engineering, 2023.

38. Lighthill, Michael James. "On sound generated aerodynamically II. Turbulence as a source of sound." Proceedings of the Royal Society of London. Series A. Mathematical and Physical Sciences 222.1148 (1954): 1-32.

39. Liu, Jiawei, "SIMULATION OF WHISTLE NOISE USING COMPUTATIONAL FLUID DYNAMICS AND ACOUSTIC FINITE ELEMENT SIMULATION" (2012). Theses and Dissertations--Mechanical Engineering. 9. https://uknowledge.uky.edu/me_etds/9

40. Ma, Ruolong, Paul E. Slaboch, and Scott C. Morris. 2009. "Fluid Mechanics of the Flow-Excited Helmholtz Resonator." Journal of Fluid Mechanics, March, 1–26. https://doi.org/10.1017/s0022112008003911.

41. Nelson, P.A. 1982. "Noise Generated by Flow over Perforated Surfaces." Journal of Sound and Vibration, no. 1 (July): 11–26. https://doi.org/10.1016/s0022-460x(82)80072-2.

VITA

SETH DONKIN

<u>PLACE OF BIRTH</u>

Jackson, MI, USA

<u>EDUCATION</u>

Bachelor of Science: Mechanical Engineering   August 2014 – Dec. 2018
University of Kentucky College of Engineering
Lexington, KY

<u>PROFESSIONAL POSITIONS HELD</u>

Acoustics and Vibration Engineer Intern   May 2019-August 2019
Trane
La Crosse, WI

Research Assistant   August 2019-July 2022
University of Kentucky College of Engineering
Lexington, KY

Associate Design Engineer   July 2022-July 2024
Harley-Davidson Motor Company
Milwaukee, WI

<u>CONFERENCE PROCEEDINGS</u>

Donkin, S. and Herrin, D.W., "Measurement of Sound Power Due to Flow Noise at the Outlet of a Straight Pipe," SAE Technical Paper 2021-01-1050, 2021, doi:10.4271/2021-01-1050.

Donkin, S. and Herrin D.W., "An Experimental Study of Flow Induced Noise from Perforated Tubes," Noise-Con 2022 Technical Paper

Donkin, S. and David Herrin, "Validation of the Computational Aeroacoustic Simulation of a Subsonic Jet Tailpipe Flow Noise" Noise-Con 2023 Technical Paper

<u>AWARDS</u>

Donald L. Greer Innovative Design Award   2018

Outstanding Master's Student in Mechanical Engineering   2020